

RELATIVE POSITIONING OF UNMANNED GROUND VEHICLES USING ULTRASONIC
SENSORS

Except where reference is made to the work of others, the work described in this thesis is my own or was done in collaboration with my advisory committee. This thesis does not include proprietary or classified information.

Harold Paulk Henderson, Jr.

Certificate of Approval:

Dan Marghitu
Professor
Mechanical Engineering

David Bevly, Chair
Associate Professor
Mechanical Engineering

Thaddeus Roppel
Associate Professor
Electrical and Computer Engineering

Joe F. Pittman
Interim Dean
Graduate School

RELATIVE POSITIONING OF UNMANNED GROUND VEHICLES USING ULTRASONIC
SENSORS

Harold Paulk Henderson, Jr.

A Thesis

Submitted to

the Graduate Faculty of

Auburn University

in Partial Fulfillment of the

Requirements for the

Degree of

Master of Science

Auburn, Alabama
May 10, 2008

RELATIVE POSITIONING OF UNMANNED GROUND VEHICLES USING ULTRASONIC
SENSORS

Harold Paulk Henderson, Jr.

Permission is granted to Auburn University to make copies of this thesis at its discretion, upon the request of individuals or institutions and at their expense. The author reserves all publication rights.

Signature of Author

Date of Graduation

VITA

Harold Paulk Henderson, Jr. was born in Tifton, GA on May 7, 1976. The family moved to Hattiesburg, MS while his father pursued a Ph.D at the University of Southern Mississippi. He graduated from Tift County High School in 1994 and accepted an appointment to the United States Military Academy at West Point, NY. He graduated in 1998 with a B.S. in Mechanical Engineering and was commissioned as a Second Lieutenant in the U.S. Army. He served as a Platoon Leader, Troop Executive Officer, Squadron Logistics Officer, and Troop Commander. In 2000 he married Carrie Hain Benefield who is an Environmental Scientist with URS. He has two sons, Hain and Ben. In 2006 he was selected to return to West Point to serve as an Instructor in the Department of Civil and Mechanical Engineering. During his studies at Auburn University he received a promotion to Major.

THESIS ABSTRACT
RELATIVE POSITIONING OF UNMANNED GROUND VEHICLES USING ULTRASONIC
SENSORS

Harold Paulk Henderson, Jr.

Master of Science, May 10, 2008
(B.S., United States Military Academy, 1998)

113 Typed Pages

Directed by David Bevly

In this thesis, a Global Positioning System/Inertial Navigation System (GPS/INS) is developed and applied to a tracked Unmanned Ground Vehicle (UGV) to provide estimates of position, heading, and velocity. The navigation estimator is then augmented with ultrasonic sensors to accurately determine the relative position of a pair of tracked UGVs. The estimator provides estimates on critical system parameters to allow for automation or collaboration. The capabilities of UGVs can be greatly increased through automation and collaboration of multiple UGVs. Automation reduces the operator workload and allows the UGV to continue operations during a loss of communication. Collaboration allows multiple small UGVs to accomplish tasks previously requiring a single large UGV. A microcontroller uses the ultra-precise Pulse Per Second (PPS) from the GPS to trigger the ultrasonic sensors. This configuration minimizes the problems traditionally encountered with use of ultrasonic sensors in an outdoor environment while providing additional information to the navigation estimator. Small, low cost sensors using MEMS technology are employed to minimize size and cost, providing a solution that can be implemented on current

UGVs. Experimental results are presented to compare the performance using GPS alone, GPS/INS, and GPS/INS/Ultrasonic sensors for estimating relative positions and headings of multiple UGVs.

ACKNOWLEDGMENTS

I would like to thank my advisor, Dr. David Bevly, for his support and direction during the entire process. He provided the resources and the expertise necessary to make the research a reality. I would also like to thank Dr. Dan Marghitu for his instruction in class on kinematics and Dr. Thaddeus Roppel for access to the ultrasonic sensors that were critical to the execution of the research.

My success in both this research and in class is due to the assistance, generosity and patience of the members of the GAVLAB. They provided invaluable assistance and guidance throughout the process. Without their experience and previous work, this research would not have been possible.

I would like to thank my family for their constant emphasis on the importance of education and the vital role of educators. Their support and toleration of an incessant curiosity have allowed me to achieve the level of success I currently enjoy and have a lot of fun along the way.

I would like to thank my sons, Hain and Ben, for constantly providing direction as to what is truly important in life. Regardless of how poorly the day had gone, they were always excited to see me and genuinely interested in “Dad’s robot”.

I must thank my wife for her continued support in yet another adventure. Her unwavering support during deployments, field problems, research, and the joys of parenting have kept me going and constantly remind me of how blessed I am.

Style manual or journal used Journal of Approximation Theory (together with the style known as “aums”). Bibliography follows van Leunen’s *A Handbook for Scholars*.

Computer software used The document preparation package T_EX (specifically L^AT_EX) together with the departmental style-file `aums.sty`.

TABLE OF CONTENTS

| | | |
|-----------------|---|-----|
| LIST OF FIGURES | | xi |
| LIST OF TABLES | | xiv |
| 1 | INTRODUCTION | 1 |
| 1.1 | Congressional Mandate | 2 |
| 1.2 | Prior Art | 3 |
| 1.3 | Contributions | 5 |
| 1.4 | Outline | 5 |
| 2 | OVERVIEW OF BASE MATILDA HARDWARE, INSTRUMENTATION DESIGN AND SOFTWARE ARCHITECTURE | 7 |
| 2.1 | Introduction | 7 |
| 2.2 | MATILDA | 7 |
| 2.2.1 | Mobile Base Unit (MBU) | 8 |
| 2.2.2 | Operator Control Unit (OCU) | 10 |
| 2.2.3 | Payloads | 11 |
| 2.3 | Instrumentation Design | 12 |
| 2.4 | Sensor Suite | 13 |
| 2.4.1 | GPS | 13 |
| 2.4.2 | Inertial Measurement Unit (IMU) | 16 |
| 2.4.3 | Encoder | 17 |
| 2.4.4 | Ultrasonic Sensor | 19 |
| 2.5 | Processor | 23 |
| 2.6 | Rabbit Core Module 4100 (RCM4100) | 23 |
| 2.7 | Completed Test Rig | 24 |
| 2.8 | Software | 26 |
| 2.8.1 | Dynamic C | 26 |
| 2.8.2 | C++ | 28 |
| 2.8.3 | MATLAB | 28 |
| 2.9 | Summary | 28 |
| 3 | UGV NAVIGATION ESTIMATOR | 30 |
| 3.1 | Introduction | 30 |
| 3.2 | Vehicle Model | 32 |
| 3.2.1 | Kinematic Model | 35 |
| 3.3 | Estimator | 37 |

| | | |
|-------|---|----|
| 3.3.1 | Extended Kalman Filter | 42 |
| 3.3.2 | Measurement Update | 43 |
| 3.3.3 | Time Update | 44 |
| 3.3.4 | Hybrid Filter | 45 |
| 3.3.5 | Heading Wrap | 45 |
| 3.4 | Conclusion | 46 |
| 4 | RELATIVE POSITION MODEL | 48 |
| 4.1 | Introduction | 48 |
| 4.2 | State Transition Matrix | 48 |
| 4.3 | Inputs | 50 |
| 4.4 | Input Matrix | 50 |
| 4.5 | Measurements | 51 |
| 4.6 | Observation Matrix | 54 |
| 4.7 | Extended Kalman Filter | 55 |
| 4.8 | Conclusion | 56 |
| 5 | EXPERIMENTAL WORK | 57 |
| 5.1 | Introduction | 57 |
| 5.2 | Sensor Data | 57 |
| 5.2.1 | IMU | 58 |
| 5.2.2 | GPS | 59 |
| 5.2.3 | Ultrasonic Sensor | 60 |
| 5.3 | Navigation Estimator | 62 |
| 5.3.1 | Simulated Static Data | 62 |
| 5.3.2 | Simulated Dynamic Data | 65 |
| 5.3.3 | Experimental Performance | 68 |
| 5.4 | Relative Position Estimator | 73 |
| 5.4.1 | Simulated Static Lead with Static Trail | 73 |
| 5.4.2 | Simulated Dynamic Lead with Static Trail | 77 |
| 5.4.3 | Simulated Dynamic Lead with Dynamic Trail | 80 |
| 5.4.4 | Experimental Performance | 82 |
| 5.5 | Conclusion | 88 |
| 6 | CONCLUSION | 90 |
| 6.1 | Summary of Contributions | 90 |
| 6.2 | Future Work | 91 |
| | BIBLIOGRAPHY | 94 |
| | A NOMENCLATURE | 97 |

LIST OF FIGURES

| | | |
|------|--|----|
| 2.1 | Mobile Base Unit | 9 |
| 2.2 | Operator Control Unit | 10 |
| 2.3 | Manipulator Arm | 11 |
| 2.4 | Arm Axes | 12 |
| 2.5 | Printed Circuit Board | 13 |
| 2.6 | uBlox RCB-4H | 14 |
| 2.7 | IMU 605 Top and Side | 16 |
| 2.8 | Optical Encoder | 18 |
| 2.9 | Parallax Ping Ultrasonic Sensor | 19 |
| 2.10 | Ultrasonic Sensor Theory of Operation | 20 |
| 2.11 | Scenarios for Ultrasonic Measurements | 21 |
| 2.12 | Rabbit Core Module 4100 | 23 |
| 2.13 | Lead UGV Test Rig | 24 |
| 2.14 | Test Rig used to replicate Trail UGV | 25 |
| 2.15 | Test Configuration | 26 |
| 3.1 | GPS Position | 31 |
| 3.2 | Integration of Bias and Noise | 31 |
| 3.3 | Instantaneous Center of Rotation Location Comparison | 33 |
| 3.4 | Lateral track velocity of UGV during pure rotation | 34 |
| 3.5 | Tracked UGV ICR Locations | 35 |

| | | |
|------|--|----|
| 3.6 | Schematic of Robot | 35 |
| 3.7 | Relation of Course (ν), Heading (ψ), and Sideslip (β) | 41 |
| 4.1 | Description of Range and Bearing Measurement | 53 |
| 4.2 | Derivation of Bearing Measurement | 54 |
| 5.1 | Schematic Illustrating the Range and Bearing Calculation | 60 |
| 5.2 | Experimental Ultrasonic Range Measurements | 61 |
| 5.3 | Experimental Ultrasonic Bearing Measurements | 61 |
| 5.4 | Simulated Static Position Estimate | 63 |
| 5.5 | Simulated Static Heading Estimate | 63 |
| 5.6 | Simulated Static Position Error | 64 |
| 5.7 | Simulated Static Heading Error | 64 |
| 5.8 | Simulated Linear Position Estimate | 65 |
| 5.9 | Simulated Linear Heading Estimate | 65 |
| 5.10 | Simulated Linear Position Error | 66 |
| 5.11 | Simulated Linear Heading Error | 66 |
| 5.12 | Simulated Square Position Estimate | 67 |
| 5.13 | Simulated Square Heading Estimate | 67 |
| 5.14 | Simulated Chicane Position Estimate | 68 |
| 5.15 | Simulated Chicane Heading Estimate | 68 |
| 5.16 | Experimental Lead Unit Static Estimate | 69 |
| 5.17 | Experimental Trail Unit Static Estimate | 69 |
| 5.18 | Line Lead Position Estimate | 71 |
| 5.19 | Line Trail Position Estimate | 71 |

| | | |
|------|--|----|
| 5.20 | Line Lead Heading Estimate | 71 |
| 5.21 | Line Trail Heading Estimate | 71 |
| 5.22 | Elliptical Lead Position Estimate | 72 |
| 5.23 | Elliptical Trail Position Estimate | 72 |
| 5.24 | Lead Heading Estimate | 73 |
| 5.25 | Trail Heading Estimate | 73 |
| 5.26 | Simulated Static Position Estimate | 74 |
| 5.27 | Simulated Static Position Error | 74 |
| 5.28 | Simulated Static Heading Estimate | 76 |
| 5.29 | Simulated StaticHeading Error | 76 |
| 5.30 | Simulated Dynamic/Static Position Estimate | 78 |
| 5.31 | Simulated Dynamic/Static Position Error | 78 |
| 5.32 | Simulated Dynamic/Static Heading Estimate | 79 |
| 5.33 | Simulated Dynamic/Static Heading Error | 79 |
| 5.34 | Simulated Dynamic/Dynamic Position Estimate | 81 |
| 5.35 | Simulated Dynamic/Dynamic Position Error | 81 |
| 5.36 | Simulated Dynamic/Dynamic Heading Estimate | 81 |
| 5.37 | Simulated Dynamic/Dynamic Heading Error | 81 |
| 5.38 | Experimental Static/Static Position Estimate | 83 |
| 5.39 | Experimental Static/Static Heading Estimate | 84 |
| 5.40 | Experimental Dynamic/Dynamic Position Estimate | 85 |
| 5.41 | Experimental Dynamic/Dynamic Heading Estimate | 86 |
| 5.42 | Position Estimates using Navigation Estimators | 87 |
| 5.43 | Position Estimates using Relative Position Estimator | 87 |
| 5.44 | Relative Position Error on Elliptical Path | 88 |

LIST OF TABLES

| | | |
|------|---|----|
| 2.1 | MATILDA Specifications | 8 |
| 2.2 | Receiver Specifications | 15 |
| 2.3 | Inertial Measurement Unit Specifications | 17 |
| 2.4 | Effect of Temperature on Measurement | 20 |
| 3.1 | Process Noise Variances | 41 |
| 3.2 | Sensor Measurement Noise Variances | 42 |
| 5.1 | Lead Accelerometer Noise | 58 |
| 5.2 | Trail Accelerometer Noise | 58 |
| 5.3 | Lead Gyro Noise | 59 |
| 5.4 | Trail Gyro Noise | 59 |
| 5.5 | Lead GPS Noise | 60 |
| 5.6 | Trail GPS Noise | 60 |
| 5.7 | Ultrasonic Sensor Noise | 62 |
| 5.8 | Simulated and Experimental Position Standard Deviation | 70 |
| 5.9 | Simulated Static Position Estimate Error and Standard Deviation | 75 |
| 5.10 | Process Noise Covariance | 77 |
| 5.11 | Measurement Noise Covariance | 77 |
| 5.12 | Simulated Linear Estimate Error and Standard Deviation | 80 |
| 5.13 | Noise Characteristics Comparison of Estimator Position Standard Deviation | 83 |

CHAPTER 1

INTRODUCTION

Unmanned Ground Vehicles (UGV) are robotic platforms that provide an extension of human capability. They are designed to carry some type of payload, but not a human occupant. Hazardous operating environments necessitate the development of the majority of UGVs. The environments include Explosive Ordnance Disposal (EOD), search and rescue in collapsed buildings, hazardous material (HAZMAT) detection, and manipulation of nuclear fuel. The inherent risk of these environments limits the incorporation of human occupants due to the cumbersome nature of the safeguards required.

UGVs can be classified by the manner in which they are controlled [11]. Tele-operated UGVs receive guidance instructions via a communications link from an operator. The link may be a physical connection such as a wire or fiber optic tether; wireless connection; or a combination of the two. The simplest example would be a toy radio controlled car which is entirely dependent on instructions from the controller.

Autonomous UGVs use onboard sensors to gather information about their surroundings and then determine the appropriate action to take. These sensors include accelerometers, gyroscopes, range finders (laser, ultrasonic, radar, camera), odometers, and GPS receivers. There are multiple examples of this type of UGV including the entries for the Defense Advanced Research Projects Agency (DARPA) Urban Challenge that navigate through an urban environment without operator input [10]. This classification should not be confused with automated UGVs whose path is predetermined via a mechanical rail or fixed trail of magnetic sensors [11].

Supervisory Control is a combination of the two previous classifications [11]. Inputs from the operator and the onboard sensors are used by the UGV to determine the appropriate output. This approach is used by the Jet Propulsion Laboratory (JPL) to control the Mars Exploration Rovers [5]. Complete control is prevented by the latency due to the vast operating distances and the limited communication bandwidth. Instruction sets are transmitted that request information or changes in position. The rover then uses onboard sensors with onboard algorithms to determine the best course of action to accomplish the instruction set.

1.1 Congressional Mandate

The importance of UGVs has received additional emphasis in the form of a Congressional mandate in the National Defense Authorization Act for Fiscal Year 2001. The mandate established a goal that unmanned, remotely controlled technology be fielded so that one-third of the operational ground combat vehicles are unmanned by 2015. DARPA staged three separate races to further the technologies needed to achieve this goal. The first DARPA Grand Challenge was held in 2004 over a 142 mile desert course. No vehicle successfully completed the entire course. The second DARPA Grand Challenge was held in 2005 where four vehicles successfully completed a 132 mile course in the required 10 hours. The DARPA Urban Challenge was held in 2007 and featured a mock urban environment requiring vehicles to interact with other vehicles while obeying traffic control devices.

The technologies developed for primarily military applications are trickling into commercial areas and even into homes. iRobot has successfully marketed UGVs for use by consumers in their homes. They can vacuum, mop or even clean gutters. These robots are

very simple, but learn and perform an assigned task with little or no human interaction [13]. Low cost sensors coupled with improving battery technology are allowing UGVs to accomplish an ever increasing list of tasks.

1.2 Prior Art

The integration of GPS and IMU measurements for land navigation has been well studied and implemented in a variety of forms [1]. The bias free measurements from the GPS compliment the higher rate measurements from the IMU. Improving the reliability and the accuracy of the estimators has taken several different paths. An obvious approach is to use more accurate GPS receivers, Differential GPS (DGPS), and higher grade IMUs, tactical and navigation grade [12]. A second approach improved performance of the estimator by augmenting the GPS/IMU measurements with map data and additional sensor measurements [18]. These approaches focused on an estimator for a single system. An alternate approach was presented and evaluated for localization of a group of robots using a distributed Kalman Filter [21]. This approach used varying sensor configurations on each robot in the group to minimize hardware requirements without sacrificing performance, while spreading the calculations for the filter over several processors. These approaches have provided performance gains, but have significantly increased the cost or the complexity of system required to implement the approach.

Modeling of small UGVs has focused primarily on wheeled differential drive vehicles in an indoor environment [6][11][27]. The complexity of modeling the dynamics of a tracked UGV can be attributed to the highly nonlinear interaction between track and terrain. One approach for use on small UGVs focused on a dynamic model based on the Instantaneous

Center of Rotation [16]. This research used experimental identification to calculate parameters based on a given UGV configuration and operating surface. This provided reasonable results as long as the operating conditions for the UGV remained constant. A second approach used finite element analysis to simulate the interaction between the track and terrain of a M113 Armored Personnel Carrier [22]. This approach incurred a tremendous computational burden and is not conducive to a real time application on a small UGV.

Since GPS became operational, its use has continually expanded from just providing position measurements. Ultra-precise timing is necessary for the system to calculate the user's position. GPS receivers provide time measurements via the output messages and through the Pulse Per Second signal. The correct GPS receiver can provide time measurements accurate to 10 ns world wide. A typical OEM receiver with an antennae uncertainty of 10 m will provide a measurement accurate to 100 ns [15]. The GPS receiver provides an ultra precise time measurement that is virtually free of drift and with a bias sufficiently small to be neglected for most applications.

Ultrasonic sensors provide a simple method to measure distance without physical contact. Ultrasonic sensors have successfully been used to detect and avoid obstacles for the last 20 years [7]. The simplicity of the sensor allows for ease of implementation but limits the accuracy and reliability in certain situations [14]. The use of various filters including the Kalman Filter has improved the accuracy of the measured time of flight, and ultimately the distance measured [2]. Research has also extended the use of the ultrasonic sensor outside by modulating the output noise [26]. The approach uses a Code Division Multiple Access approach to allow multiple sensors to operate at the same time in close proximity without sacrificing reliability.

1.3 Contributions

This thesis developed and tested a concept that used ultrasonic sensors triggered by GPS receivers to provide relative measurements on a pair of UGVs. The proposed configuration was shown to reliably provide these measurements. The resulting measurements were then used to estimate position and heading. A summary of the specific contributions provided in this thesis are listed below.

- Designed and implemented IMU/GPS sensor suite for tracked UGV
- Developed tracked UGV navigation estimator
- Developed method to trigger ultrasonic sensors with GPS PPS to reliably measure relative position and orientation of UGV
- Examined the accuracy of position and heading estimates of navigation and relative position estimators using simulated and experimental data
- Compared performance gains achieved in relative position and heading estimates using relative measurements

1.4 Outline

Chapter 2 provides an overview of the hardware and software used to implement the relative position estimator. Each sensor is presented and the manufacturer's published performance parameters are presented for comparison. Images of the components are provided to convey the size of the sensors and the completed sensor suite. The separate software packages and their implementation are covered in this chapter as well. The designation assigned to each program and the function it serves is also explained.

Chapter 3 gives an overview of Kalman and Extended Kalman Filters in addition to the navigation estimator developed for a single UGV. The kinematic model used for the EKF is presented with justification for its selection over a dynamic model. The equations used for the model are provided, and the process used to create the matrices necessary to implement the EKF for a navigation estimator are shown.

Chapter 4 expands the navigation estimator from a single UGV to include both UGVs as well as additional measurements. The implementation of the ultrasonic sensors to measure range and bearing is shown along with the equations defining the measurements. The matrices necessary to implement the EKF are derived and presented.

Chapter 5 covers the testing with simulated and experimental data used to evaluate the performance of the EKF. Each sensor is evaluated to measure the unique noise characteristics for inclusion in the EKF. Simulated results are presented to demonstrate the ideal performance of both the navigation and relative position estimator. Experimental results using measurements from the sensor suites are presented to demonstrate the improvement through the use of the ultrasonic sensors.

Chapter 6 presents the conclusions from the research. The goals for the thesis are evaluated and areas of future work are identified and discussed. The areas of future work include alternative methods to implement the EKF, implementation in realtime, additional sensors, and increasing relative measurement rates.

CHAPTER 2

OVERVIEW OF BASE MATILDA HARDWARE, INSTRUMENTATION DESIGN AND SOFTWARE ARCHITECTURE

2.1 Introduction

This Chapter presents the UGV hardware, instrumentation and software architecture used for the design and implementation of the navigation and relative position estimator. The goal of the research is to augment the sensors necessary for a navigation estimator with ultrasonic sensors to provide relative measurements between a pair of UGVs. The relative measurements are used to refine the estimated states of both UGVs, allowing the UGVs to maintain a desired formation or orientation. The research focuses on improving the performance of the navigation estimator without the reliance of more expensive sensors or a significant increase in computational burden.

2.2 MATILDA

The UGV used for testing purposes was produced by Mesa Robotics for the Unmanned Ground Vehicle/Systems Joint Program Office (UGVS/JPO) at Redstone Arsenal, AL. Mesa Associates' Tactical Integrated Light-Force Deployment Assembly (MATILDA) was developed as a man-portable teleoperated UGV for a variety of missions. These missions included reconnaissance, surveillance, remote breach, improvised explosive device (IED) disposal, casualty recovery, and Nuclear Biological Chemical (NBC) detection [17]. Table 2.1 provides the dimensions and capabilities of the system.

Table 2.1: MATILDA Specifications

| | |
|------------------------|---|
| Size | 50.8 cm x 30.48 cm x 66.04 cm |
| Platform Weight | 20 kg w/o Batteries 25.4 kg with Batteries |
| Batteries | 4x12 Vdc |
| Speed | 0.9144 m/s |
| Operating Time | 4 - 6 hrs |
| Payload Bay Dimensions | 34.29 cm x 41.91 cm |
| Payload Capacity | 56.7 kg |
| Towing Capacity | 215 kg |
| Cameras Drive | Dual Camera Assembly Color plus Black & White |
| Cameras Rear | Fixed Black & White |
| Fording Depth | 15.24 cm |
| Control Range | LOS 1.0 km Tunnel Crawl-In 50 m Tunnel Walk-In 100 m Tunnel Drive-In 600 m |

2.2.1 Mobile Base Unit (MBU)

The MBU shown in Figure 2.1 is a tracked robotic vehicle that serves as the base for the additional implements such as a manipulator arm, Nuclear-Biological-Chemical (NBC) detector, or recoilless disrupter. The MBU can be used in a standalone configuration or with the additional implements. The MBU is operated via a radio frequency (RF) link or a fiber

optic (FO) link with a 200 m cable. The data links passes instructions from the Operator Control Unit (OCU) to the MBU and returns audio and video feeds from the MBU for the operator. The MBU has three on board cameras for the operator. The operator can pan and tilt the forward looking black/white and color cameras. A fixed camera provides a rear view to aid in maneuvering the vehicle and maintaining situational awareness.

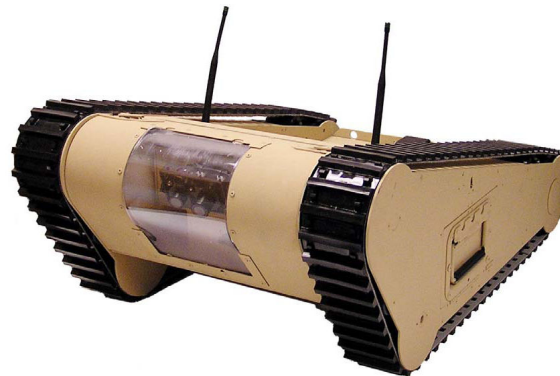


Figure 2.1: Mobile Base Unit

The suspension has two fixed road wheels in front and back with two intermediate road wheels per side that are mounted on spring loaded arms. The majority of the weight is born by the front and rear road wheels. This fixed suspension is adequate for the relatively small size and a maximum speed of 0.9 m/s. Over uneven terrain, the MBU may exhibit erratic steering since the track cannot conform to the ground profile. Separate direct current motors power each track through a reduction gearbox attached to a drive sprocket. The MBU uses pulse width modulation (PWM) to control the motor speed but has no feedback loop to control track speed. The inherent friction imparted by the gear box and track make slow speed maneuvering difficult. The user must apply sufficient throttle input to “break loose” the MBU then reduce it to prevent unwanted acceleration.

2.2.2 Operator Control Unit (OCU)

The OCU shown in Figure 2.2 serves as the interface for the user. It presents the audio and video links to the operator and accepts the inputs from the user. A single joystick is used to control the direction and the speed of the MBU. A separate joystick is used to pan and tilt the forward looking camera with rocker switches used to control camera settings such as zoom and iris. A rotary switch selects the camera view displayed on the monitor. Two additional joysticks are used to control the manipulator arm. The arm contains five degrees of freedom allowing a full range of motion. A key is used to control the firing circuit that can be used to initiate breaching charges or the recoilless disruptor.



Figure 2.2: Operator Control Unit

The controls are logically arranged but require a great deal of practice to develop proficiency in operating the MBU with only the provided video and audio cues. The workload of the operator can be quite high and could be significantly reduced by automating processes, such as way point navigation or control of the manipulator arm.

2.2.3 Payloads

The main payload of the MBU is the manipulator arm shown in Figure 2.3. The arm provides the operator with the capability to manipulate objects within one meter of the MBU. The arm's maximum lift is 6.80 kg at full extension and increases to 15.87 kg as the arm is retracted toward the MBU. The arm incorporates two additional cameras and a search light. One camera is located directly above the gripper for use in aligning the gripper. A second camera incorporates a color camera with an 18x zoom lens. The search light provides both white and infrared (IR) light for use in a variety of environments.

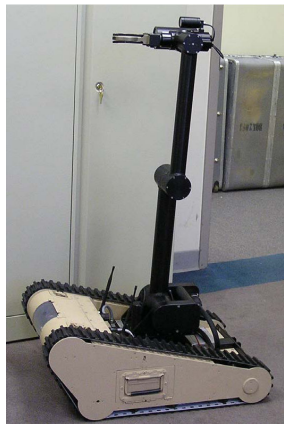


Figure 2.3: Manipulator Arm

The five degrees of freedom of the manipulator arm are shown in Figure 2.4. The joints are best described by the analogous human joints: waist, shoulder, elbow, and wrist. Smooth operation of the arm to manipulate objects requires a great deal of practice to develop proficiency. The lack of depth perception when viewing objects through the on board

cameras further complicates the process. Multiple cameras located at different points provide the capability to judge distance; however, the operator must manually switch between the cameras to accomplish this task.

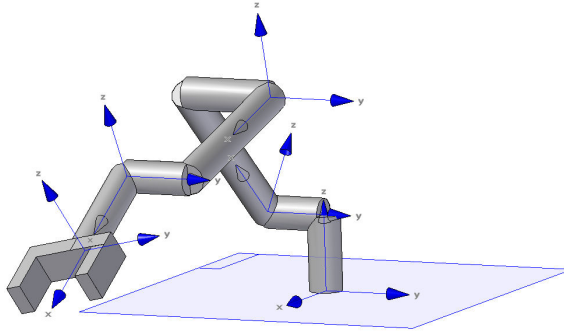


Figure 2.4: Arm Axes

2.3 Instrumentation Design

The MATILDA provided the test bed for this research but could not provide any measurements of platform dynamics for implementation of the navigation and relative position estimators. The MATILDA was retrofitted with sensors to provide these measurements. The UGVs were on loan and installation could not to damage the UGV or degrade performance. Only commercially available sensors were considered to reduce cost and development time. An interface was developed to integrate and record the measurements for use by the estimator. These additions provide an instrumented UGV capable of providing the measurements and inputs necessary to implement a navigation estimator. The instrumentation package was duplicated to replicate a second UGV, thus providing the relative measurements required for the research.

2.4 Sensor Suite

The size of the robot requires a small dedicated sensor suite that incorporates the necessary sensors, communication hardware, and computing power capable of being carried by the MBU without degrading capability. A microcontroller and MEMS based sensors were selected to meet both size and budgetary constraints. A printed circuit board (PCB) shown in Figure 2.5 was designed and developed that provides a common interface for all sensors. The PCB receives the necessary measurements and the onboard microcontroller performs the necessary operations for use by the estimator.

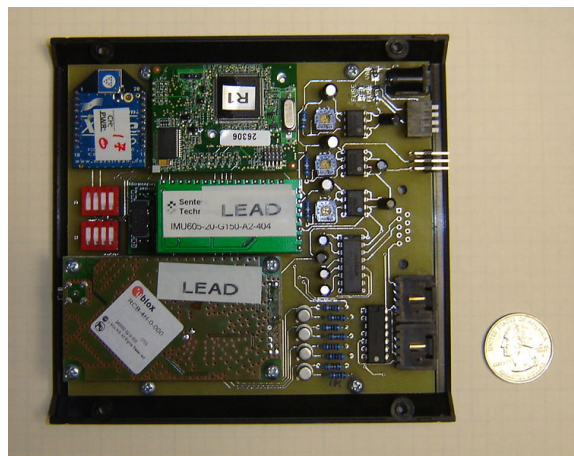


Figure 2.5: Printed Circuit Board

2.4.1 GPS

The uBlox RCB-4H GPS receiver shown in Figure 2.6 is a small yet relatively accurate receiver that can easily be incorporated into the sensor suite. The actual receiver is the size of a postage stamp and is a surface mount device. The RCB-4H consists of the receiver mounted on a printed circuit board that incorporates an antennae receptacle and a standard

Table 2.2: Receiver Specifications

| Parameter | Value |
|-----------------|--------------------------|
| Channels | 16 |
| Position | 2.5 m CEP |
| Position w/SBAS | 2.0 m CEP |
| Update Rate | 4 Hz |
| Cold Start | 34 s |
| Reacquisition | 1 s |
| Timing Accuracy | rms 50 ns 99% < 100ns |

The GPS receiver also provides a Pulse Per Second (PPS) which is a digital signal that is synchronized with GPS time. The PPS provides a convenient method to synchronize multiple devices. GPS provides the capability of time comparison with an accuracy measured in nanoseconds. The accuracy of the time comparison is a function of the accuracy of the position where the comparison is made. With antennae coordinates having an uncertainty of 10 m, the accuracy is 100 ns [15]. The PPS output is most often used to synchronize IMU measurements with the corresponding position measurements. This research will also use it to synchronize the ultrasonic sensors. In comparison, the accuracy of the real time clock on the microcontroller is 150 ns [20]. The additional benefits of using the GPS measurement, are the corrections GPS uses to minimize drift and bias in the receiver clock and synchronization of the receiver clock to a common time. An elaborate scheme would be necessary to synchronize the real time clocks of multiple microcontrollers without the use of the GPS

measurements. Drift between the microcontroller's clocks would introduce a bias into the ultrasonic measurements.

2.4.2 Inertial Measurement Unit (IMU)

A Sentera Technology IMU was selected to provide the required measurements of platform acceleration and rotation. The IMU 605 shown in Figure 2.7 is a six degree of freedom IMU based on Analog Devices MEMS components. The IMU incorporates the accelerometers and gyroscopes into a single package that significantly simplifies implementation. The IMU also compensates for temperature effects on the MEMS sensors and outputs the data via a standard serial port. Also, the IMU synchronizes its measurements using the Pulse Per Second (PPS) provided by the GPS receiver, which simplifies data alignment. The IMU has the capability to measure acceleration in three separate axes and roll rates about the same axes. Only one accelerometer and one rate gyro measurement are used since the robot is constrained to a level plane for this thesis. Based on the constraint imposed by the level plane the UGV is not allowed to tilt or roll due to its fixed suspension. A more robust model and avenue for future research, would require the inclusion of the additional measurements to allow the model to compensate for roll, pitch, and yaw.

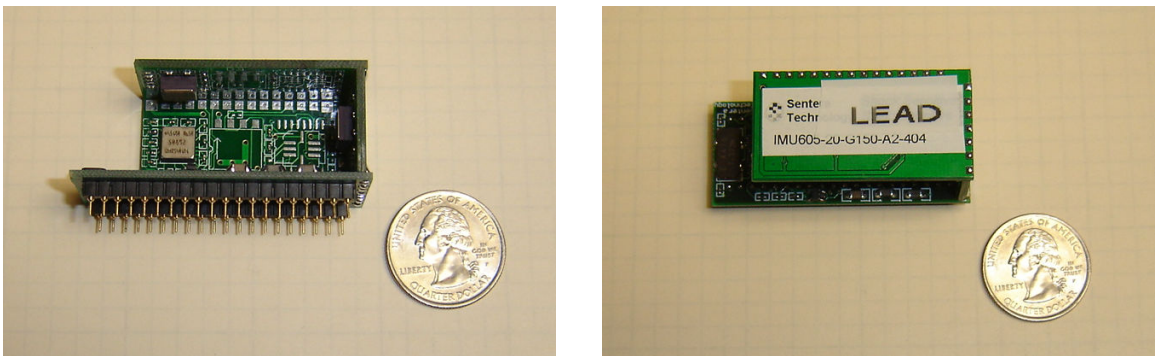


Figure 2.7: IMU 605 Top and Side

The MEMs sensors are inexpensive, small, and require very little power to operate; however, the devices do not have the precision necessary for standalone navigation. The IMU performance specifications are shown in Table 2.3. Integration of the rate measurements would lead to a navigation solution that would grow without bound. The high update rate of the IMU compliments the unbiased measurements of lower update rate GPS. The IMU measurements provide measurements of system dynamics when GPS measurements are not available.

Table 2.3: Inertial Measurement Unit Specifications

| Parameter | Value |
|---------------------|----------------------------|
| Digital Output Rate | 60 Hz |
| Angular Rate | |
| Range | $\pm 150 \text{ deg/s}$ |
| Bias | $\pm 1 \text{ deg/s}$ |
| Resolution | $< 0.025 \text{ deg/s}$ |
| Acceleration | |
| Range | $\pm 19.62 \text{ m/s}^2$ |
| Bias | $\pm 0.1472 \text{ m/s}^2$ |
| Resolution | $< 0.002943 \text{ m/s}^2$ |

2.4.3 Encoder

The MATILDA originally had no means to measure track speed or position. Optical encoders were retrofitted to the MATILDA at the drive sprocket in order to measure track

position for this research. The velocity can then be calculated by averaging the track positions. The resulting measurements include a small amount of error due to quantization. The variance of the quantization error is approximated as $\sigma^2 = \frac{q^2}{12}$ where q is the quantization step size [24]. The calculated variance for the velocity measurements is 0.0008 m/s. This value is an order of magnitude smaller than the variance of the velocity measurement from GPS receiver.

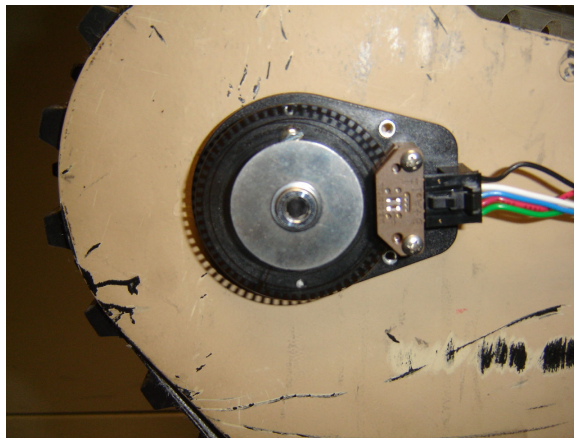


Figure 2.8: Optical Encoder

The US Digital E6S-64I optical encoder is appropriate for this application due to its small size and ease of operation. The encoder has a resolution of 64 cycles per revolution(CPR). This resolution coupled with the use of the quadrature decoder on the RCM4100 allowed the position of the track to be measured to ± 1.4 degrees. This angular measurement corresponds to ± 9.36 cm based on the diameter of the drive sprocket. An additional advantage of using the 64 CPR encoder is that a single byte counter in the RCM4100 can be used to measure a complete revolution. The limit of the counter's size for the RCM4100's

quadrature decoder prevented the use of higher resolution encoders at the MBU's operating speed.

2.4.4 Ultrasonic Sensor

In order to measure the relative distance between UGVs and their orientation an ultrasonic sensor was needed. The Parallax Ping ultrasonic sensor shown in Figure 2.9 incorporates an ultrasonic transducer, receiver, and timer into a single module allowing for non-contact measurement with a range of two centimeters up to two meters. The module is ideal based on reliability, cost, and ease of use. A three pin connector is used to provide power, ground, and input/output(I/O).

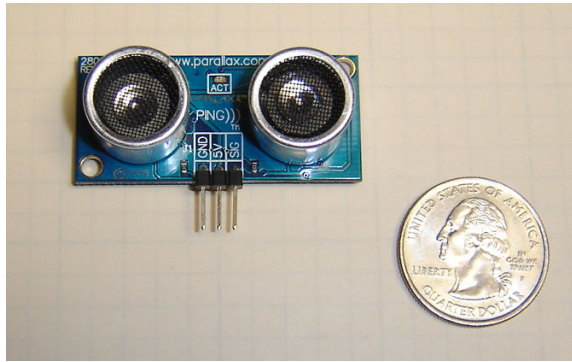


Figure 2.9: Parallax Ping Ultrasonic Sensor

The theory of operation is depicted in Figure 2.10. The RCM4100 generates a pulse on the I/O pin for 2 to 5 μs . The Ping sensor waits 750 μs then emits an ultrasonic burst and generates a pulse on the I/O pin. The Ping holds the I/O pin high until the echo of the burst is detected. The length of the pulse is proportional to the distance traveled by the sound wave. The maximum wait time is 18 ms to prevent the sensor from hanging up

should no return be received. This time equates to a round trip distance of approximately 6 meters.

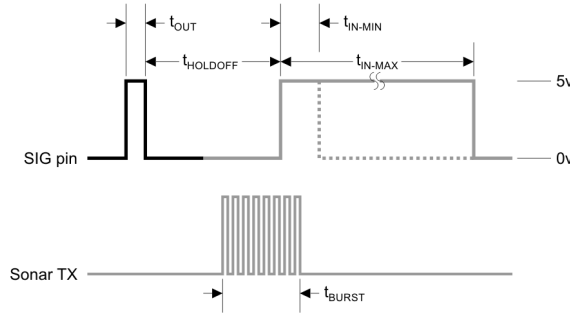


Figure 2.10: Ultrasonic Sensor Theory of Operation

The speed of sound can be approximated as $c_{ideal} = \sqrt{kRT}$. The ideal speed of sound at 70 degrees F is 343.85 m/s. Testing was conducted from 50 degrees F to 90 degrees F. Temperature variation over this window represents a change of only ± 2 percent and therefore was neglected. Table 2.4 shows the effect of varying temperatures on measured distances.

Table 2.4: Effect of Temperature on Measurement

| Temperature | Actual Distance | Mean Measured Distance | Difference |
|-------------|-----------------|------------------------|------------|
| 51 F | 1.334 m | 1.307 m | -2% |
| 70 F | 1.334 m | 1.332 m | -0.1% |
| 89 F | 1.334 m | 1.357 m | +1.7% |

The Ping sensor is designed for use on small robots for proximity detection. Graphical depictions of the manner of operation of the sensor are shown in Figure 2.11. Ideally the object that reflects the burst is flat and perpendicular to the path of propagation. When

the angle between the path of propagation and smooth surface are less than 45 degrees no energy is reflected for the sensor to detect. An object that is too small may reflect a portion of the energy, but this reflected energy is below the threshold set for detection.

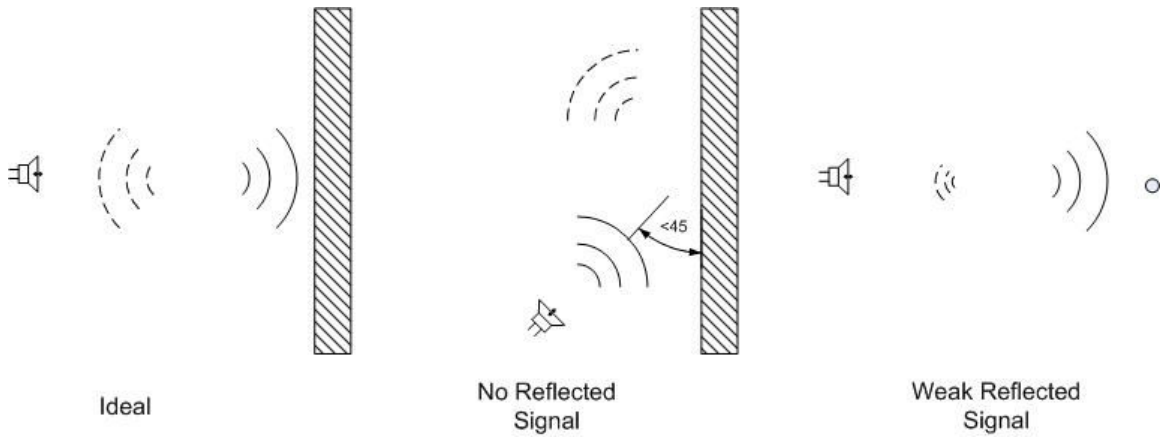


Figure 2.11: Scenarios for Ultrasonic Measurements

The frequency of the signal is the controlling factor in the size of object that can be readily detected. The wavelength of the sound wave should be comparable to the irregularities on the reflecting surface [14]. The required wavelength of the ultrasonic burst based on a specified feature size is presented in Equation (2.1).

$$\begin{aligned}
 \lambda &= \frac{c}{f} & (2.1) \\
 \lambda &= \frac{343.85m/s}{40000Hz} \\
 \lambda &= 8.5mm
 \end{aligned}$$

The sensor can be expected to detect objects larger than 8.8mm given the 40kHz operating frequency. Therefore the sensor should reliably detect the sister UGV based on the size of the MATILDA.

The simplicity of the sensor is offset by limitations inherent to most ultrasonic sensors. Echoes from other sensors may provide false readings as the sensor has no way to determine the origination of the echo. The use of the PPS to trigger both sensors will exploit this limitation. 99% of the PPS signals are accurate to within 100 ns. This corresponds to a distance error of $\pm 3.45cm$.

Research has shown that the burst for the sensor may be modulated with a digital signal [26]. The use of convolution allows a comparison of the transmitted signal with the echo to minimize faulty readings. This approach improves the reliability from 11% to 92% in a noisy environment with the frequency of the noise matching the transmitted signal. In addition to improving reliability, it also allows multiple sensors to operate simultaneously in close proximity [26]. The study used a dedicated transducer emitting white noise at the ultrasonic frequency to simulate a noisy environment.

The constraints previously illustrated in Figure 2.11 are overcome by using the GPS PPS as a precision timing device. The common time removes the need to differentiate between multiple echoes and does not use reflected signals. The use of a common time to trigger the sensors, in this case GPS time, allows the sensor to measure the time it takes the other UGV's burst to reach its position instead of waiting for the echo. The signal from the sister UGV has a much higher intensity and is not susceptible to multi path assuming a clear line of sight is available between the UGVs.

2.5 Processor

The Rabbit Core Module 4100 shown in Figure 2.12 was selected for the processor to use on the PCB. The RCM4100 incorporates a 58 MHz microcontroller with 512 KB of memory and several hardware capabilities that simplify the incorporation of the sensors. The RCM4100 has dedicated serial ports that allow the IMU and GPS to directly provide digital measurements. The serial ports also allow the RCM4100 to output data via a radio modem and serial connector. The input capture function allows the RCM4100 to precisely measure the time of flight for the ultrasonic ping. The input capture counter is configured for 1 *ns* per count. The integral quadrature decoder allows the RCM4100 to calculate the track speed and direction using standard optical encoders.

2.6 Rabbit Core Module 4100 (RCM4100)

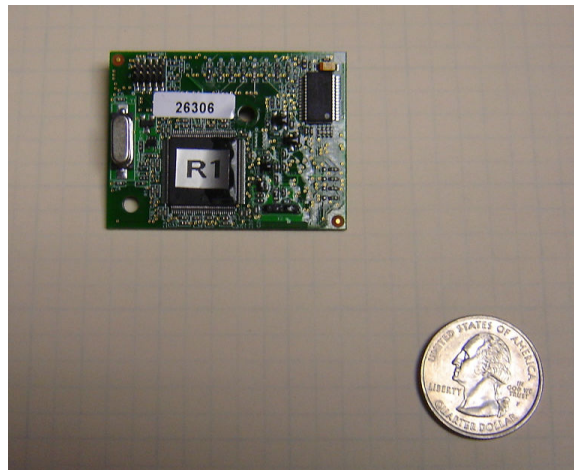


Figure 2.12: Rabbit Core Module 4100

Rabbit Semiconductor developed a proprietary programming language, Dynamic C, to control the RCM4100. Dynamic C combines the functionality of C with built in mnemonics to control the hardware functions unique to the RCM4100. A relatively simple program was developed to receive the measurements from each sensor, parse the messages to extract the necessary values and then output the information needed to implement the estimators.

2.7 Completed Test Rig

A suitable platform to mount the sensors was required for testing. A rigid aluminum frame shown in Figure 2.13 was constructed to mount the sensors and allow for installation in the payload bay of the MATILDA. The frame provided the necessary offset to prevent interference between the body of the MATILDA and the ultrasonic sensors. The IMU was located at the center of gravity in the East North plane to minimize any lever effects the IMU might experience during rotation. The height of the frame offset the IMU in the Up direction but was neglected due the constraint imposed by operation on flat level surfaces.



Figure 2.13: Lead UGV Test Rig

A leader-follower scenario was used for experimental testing to simplify implementation and ease comparison of results. A second platform was constructed to replicate the trail UGV rather than using two separate UGVs for testing. The location of the IMU and GPS antennae on the trail unit match the dimensions present on the lead platform. The platform shown in Figure 2.14 was attached to the lead UGV via a hitch. This configuration allowed for the orientation and distance between the UGVs to be controlled and accurately measured. The sensor suites from both UGVs would undergo similar dynamics during testing, but would be recorded by their respective sensors.



Figure 2.14: Test Rig used to replicate Trail UGV

The sensor platforms are used in conjunction for static and dynamic testing. The tongue of the trailer is marked with the effective distance between the center of gravity of both platforms. A protractor provides a convenient method to verify the measured bearing between the lead and trail platform. The aluminum frame was selected due to its light weight, exceptional rigidity and low cost. Figure 2.15 shows the lead MATILDA with trail sensor following at 2.431 m.

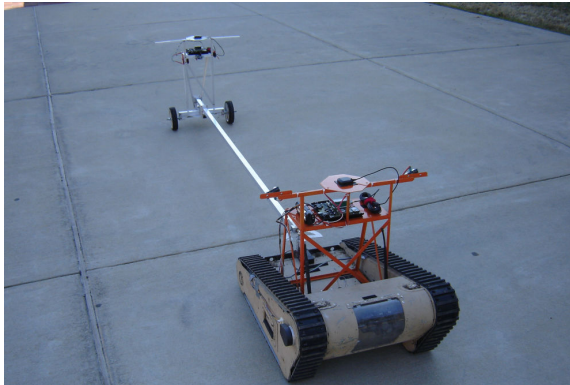


Figure 2.15: Test Configuration

2.8 Software

The software developed for this research is divided into three separate categories. The programs are delineated by language used and also location employed. The sensor suite on the UGV uses Dynamic C, a C++ routine runs on the PC to parse and log data, and MATLAB is used for data analysis.

2.8.1 Dynamic C

A simple program was implemented on the RCM4100 that incorporated several parsing subroutines. The IMU outputs data at 60 Hz as a constant stream. The RCM4100 determines the start of each message and stores the measurement. The outputs from the IMU are scaled and must be multiplied by the scale factor to provide measurements in the appropriate units. The RCM4100 outputs all sensor measurements to the serial port with the receipt of each new IMU message. The IMU message serves as the trigger since it has

the highest update rate. This approach yields duplicate GPS and Ultrasonic Measurements that are discarded during post processing.

The GPS receiver outputs data at 4 Hz in the National Marine Electronics Association (NMEA) Recommended Minimum (RMC) format. The message is parsed for Coordinated Universal Time (UTC), Latitude, Longitude, velocity, and heading. The parser also verifies the measurements received are valid via the flag field in the RMC format.

An Interrupt Service Routine (ISR) is implemented with the input capture subroutine on the RCM4100. This routine is time critical and must be executed as soon as the PPS is received. The use of the ISR allows the RCM4100 to execute the routine within 24 ticks of the clock on the RCM4100. The maximum delay is $0.4 \mu s$ based on the 58 MHz processor. The ISR was written to minimize the time required to run, thus preventing conflicts with the other routines.

The quadrature decoder counter is read and reset with each IMU measurement. This output rate ensures that the counter does not overrun, leading to possible loss of data. Left and right track measurements are recorded to allow for determination of both velocity and yaw rate. The resolution of the encoder and counter do introduce quantization error, but these values are extremely small and accounted for in the estimator.

Dynamic C does not have the capability to perform the matrix operations required directly. The operations can be decomposed into the individual algebraic operations; however, this approach would require significant software development. Therefore a two way radio modem is employed to allow the PC to execute programs developed in C++. The application used in this thesis is run post-process. An avenue of future research would be implementation in real-time.

2.8.2 C++

A stand alone application was created for use on a laptop to receive the measurements output from the RCM4100. The application sets up and opens the serial ports to allow the measurements to be received and saved to a standard text file. The application displays the measurements or writes them to a file for later analysis. The application also provides a command link to the RCM4100 and ultimately the MBU.

2.8.3 MATLAB

All analysis was conducted post-process in MATLAB to simplify the development process. Real-Time Workshop is available to execute MATLAB code in real-time. Converting the algorithm into a real-time application exceeds the scope of this research. Once the algorithms have been validated and verified, future research would incorporate them into a real-time application.

2.9 Summary

This chapter presents the hardware, instrumentation and software necessary to implement a navigation and relative position estimator. The MATILDA represents UGVs currently in use with the typical capabilities and limitations. The sensors traditionally used to implement a navigation estimations are presented in addition to the ultrasonic sensors that will provide the relative measurements. A simple yet effective estimator can be constructed with commercial off the shelf (COTS) components with relative ease. The only custom parts required were the encoder mount and the printed circuit board and both were

acquired commercially. The incorporation of these components will allow the UGV to estimate its position using the algorithms developed in the following chapter. The prototype device does not appreciably increase the size or cost of the UGV and does not degrade payload while providing a new capability.

CHAPTER 3

UGV NAVIGATION ESTIMATOR

3.1 Introduction

The first problem that must be solved is the determination of the robot's location with respect to some reference frame. This reference frame may be defined many different ways. Ideally a common reference frame is chosen to allow for ease of comparison to positions of interest, i.e. the desired end point, obstacle, or partner robot. The reference frame selected is determined by the area of operation as well as the dynamics of interest. Aircraft operate over large distances and rely on Latitude, Longitude, and Altitude. UGVs traditionally operate over relatively small areas measured in meters to kilometers, and thus an East, North, Up reference frame is more useful. Regardless of the reference frame chosen, the sensor measurements must be evaluated to determine the robot's absolute position. A single sensor may be used to determine the position; however, the resulting solution will be limited by the quality of the sensor used.

Although GPS provides a bias free measurement, the position measurements will fall within a 10 meter radius using a single receiver [19]. The higher the quality of the receiver, the lower the standard deviation of those measurements. For example, the uBlox error has outliers out to 10 meters, but half are clustered within 2 meters of the actual point. A plot of calculated positions is shown in Figure 3.1 to illustrate the point. The plot shows data taken over a 15 minute period.

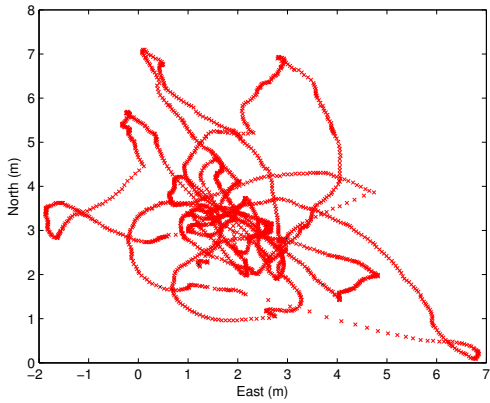


Figure 3.1: GPS Position

This level of accuracy is sufficient for navigation on the macro scale, but is lacking when attempting to determine multiple UGV locations in close proximity. Additionally the use of only the MEMS IMU is effective over very short periods of time. Integration of the noise on the measurements causes the error in the navigation solution to grow without bound [4]. Figure 3.2 illustrates the effect of integrating a sensor bias, zero mean white noise, and the combination of the two over a two second period.

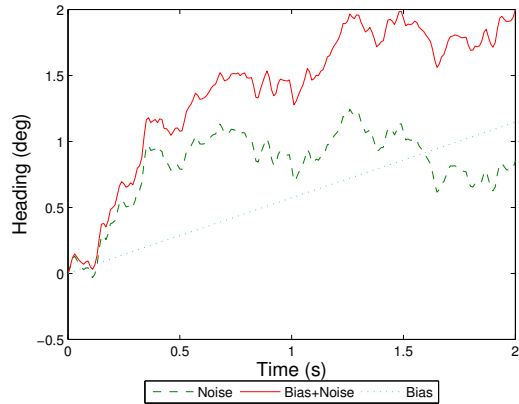


Figure 3.2: Integration of Bias and Noise

The combination of multiple sensors allows for a complementary solution to be developed for the entire system. The manner in which they are integrated has been widely studied and each configuration provides a slightly different capability. One approach focused on using inertial measurements to update position estimates between low rate (1-5 Hz) GPS measurements [9]. The IMU provides measurements of system dynamics between the GPS measurements. Another focused on using the inertial measurements during GPS outages [3]. This approach relied heavily on the GPS and used the IMU only during GPS outages. A third approach combined the two approaches and augmented GPS with inertial measurements [1].

The system design and manner in which the estimator uses the measurements varies greatly. Cost and size are a controlling factor so a relatively simple algorithm requiring only moderate computational loads was selected. Therefore, the scheme selected for this thesis uses an Extended Kalman Filter (EKF) to evaluate the measurements provided and generate a reasonably accurate estimate.

3.2 Vehicle Model

The Kalman Filter for this research employs a kinematic model for its estimation. The kinematic model is based on the relationship between the various states and their derivatives. The relation between the states and their respective derivatives are known and can be calculated without extensive a priori knowledge. The MATILDA is a tracked UGV which would require a complex dynamic model [16] [22]. Extensive model identification would be necessary to employ such a model. The interaction between the track and the terrain

introduce numerous complexities which invalidate most assumptions used for differential drive vehicles.

The instantaneous center of rotation (ICR) for each track does not lie within the contact patch which is the case for small differential drive vehicles on smooth surfaces [23]. A comparison of ICR locations for a tracked and wheeled differential drive UGV is made in Figure 3.3. The diagram is not to scale. The contact patch for the tracked UGV is significantly larger than a wheeled UGV of comparable size and weight. The ICRs for the wheeled UGV lie within the contact patch for the respective wheel. The small area of the contact patch, and the location of the ICR ensures that all points within the contact patch lie in close proximity. This proximity allows for the assumption that no slip occurs between the tire and terrain.

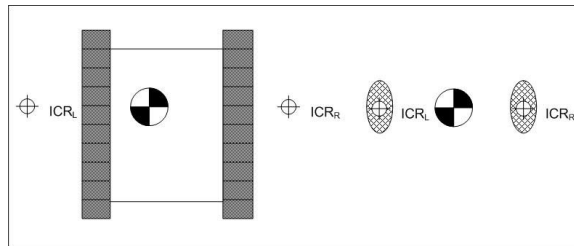


Figure 3.3: Instantaneous Center of Rotation Location Comparison

The ICRs for tracked vehicle lies outside the contact patch of the track during turns and the location is a function of the yaw rate, CG location, and coefficient of friction between the track and terrain. The larger contact area coupled with the offset of the ICR invalidates the no-slip assumption used in the wheeled model. Figure 3.4 graphically illustrates the lateral velocities along the length of the contact patch during a counter-clockwise turn. The lateral velocity increases significantly the farther the point is displaced from the lateral axis.

The lateral axis is shown as a dotted line in the figure. The no-slip assumption is only valid for tracked vehicles under purely longitudinal translation or extremely small rotation rates.

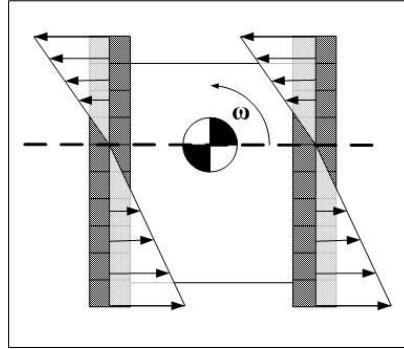


Figure 3.4: Lateral track velocity of UGV during pure rotation

One approach for modeling a small UGV used experimental identification to determine the location of the instantaneous centers of rotation given a specific UGV configuration and type of terrain. This approach imposed only a small computational burden, but required extensive experimentation [16]. A generic schematic depicting the relation of ICR for the UGV is shown in Figure 3.5. Each track rotates about an ICR identified as ICR_R and ICR_L . The ICR for the UGV, ICR , lies along the lateral axis that passes through the track ICRs and the center of gravity. The offset from the CG for the ICR is the sum of the individual track ICRs. A second dynamic model was based on finite element analysis of the track pad interaction of a M113 Armored Personnel Carrier [22]. This approach only required soil parameters for evaluation, but incurred a significant computational burden. Both of these models provide valuable insight into the dynamics of the UGV but are too complex for implementation on a small inexpensive UGV and beyond the scope of this thesis.

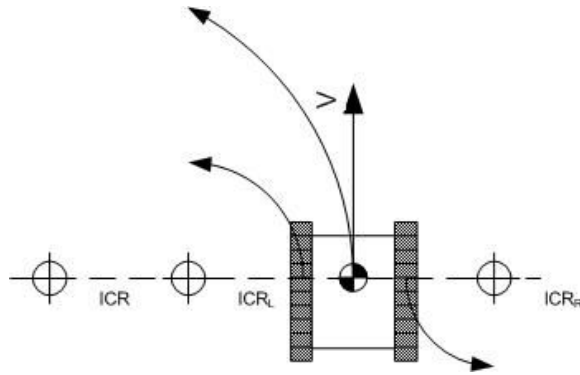


Figure 3.5: Tracked UGV ICR Locations

3.2.1 Kinematic Model

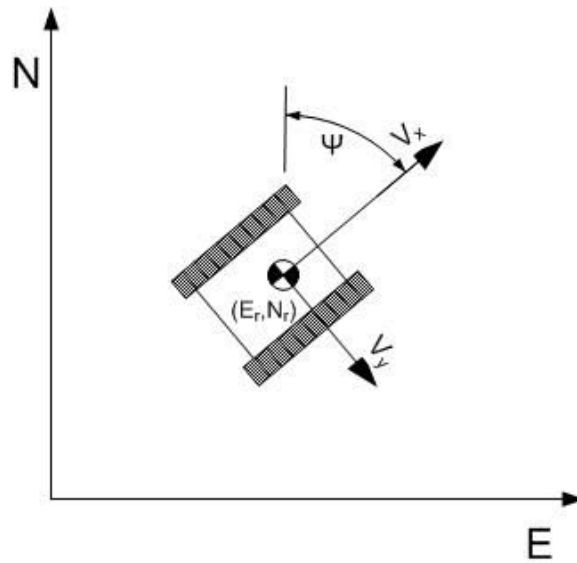


Figure 3.6: Schematic of Robot

The position of the UGV in general ENU coordinates is shown in Figure 3.6. The velocity of the UGV in terms of the longitudinal velocity, V_x , and heading, ψ is defined in

EQ (3.1).

$$\begin{aligned}\dot{\psi} &= r \\ \dot{E} &= V_x \sin(\psi) \\ \dot{N} &= V_x \cos(\psi)\end{aligned}\tag{3.1}$$

V_y is the lateral velocity at the center of gravity (CG) in a body fixed frame and is neglected for the purposes of this research due to the UGV's relatively slow speed. The maximum speed of the MATILDA is 0.9144 m/s on smooth terrain with a full battery charge. The maximum speed observed during testing never exceeded 0.9 m/s. The magnitude of any potential lateral velocity would be below the noise floor of the sensors used for calculations. The additional complexity of the computations required to account for lateral velocity would not yield an appreciable improvement in the fidelity of the model.

The model dynamics in Equation (3.1) are of the form:

$$\dot{x} = f(x) + Bu\tag{3.2}$$

where the states selected for this model are:

$$x = [V_x \quad \psi \quad N \quad E]^T\tag{3.3}$$

3.3 Estimator

Equations(3.1) must be placed in the following form to allow the use of linear state space estimation:

$$\dot{X} = AX + Bu \quad (3.4)$$

$$Y = CX \quad (3.5)$$

Because both sensor inputs are biased, the fourth order model described defined by Eq (3.1) must be augmented with two additional states resulting in a sixth order estimator. The two additional states are the accelerometer bias a_b and the rate gyro bias g_b . The six resulting estimated states are:

$$\hat{X} = [\hat{V}_x \quad \hat{a}_b \quad \hat{\psi} \quad \hat{g}_b \quad \hat{N} \quad \hat{E}]^T \quad (3.6)$$

The dynamics in Equation (3.1) must be linearized about a given point due to their nonlinear nature in order to employ the planned state space estimation. The state equations are linearized through the use of the Jacobian (J) at each time step. The linearized state equations are of the form:

$$\dot{X} = JX + Bu \quad (3.7)$$

The Jacobian is defined as:

$$J = \begin{bmatrix} \frac{\partial f_1}{\partial x_1} & \cdots & \frac{\partial f_1}{\partial x_n} \\ \vdots & \ddots & \vdots \\ \frac{\partial f_n}{\partial x_1} & \cdots & \frac{\partial f_n}{\partial x_n} \end{bmatrix} \quad (3.8)$$

The Jacobian based on the proposed model is listed below:

$$J = \begin{bmatrix} 0 & -1 & 0 & 0 & 0 & 0 \\ 0 & 0 & 0 & 0 & 0 & 0 \\ 0 & 0 & 0 & -1 & 0 & 0 \\ 0 & 0 & 0 & -1 & 0 & 0 \\ \cos(\psi) & 0 & -V_L \sin(\psi) & 0 & 0 & 0 \\ \sin(\psi) & 0 & V_L \cos(\psi) & 0 & 0 & 0 \end{bmatrix} \quad (3.9)$$

The input vector(u) is defined by:

$$u = \begin{bmatrix} a_{long} \\ r_z \end{bmatrix} \quad (3.10)$$

The corresponding input matrix(B) is defined for the model by:

$$B = \begin{bmatrix} 1 & 0 \\ 0 & 0 \\ 0 & 1 \\ 0 & 0 \\ 0 & 0 \\ 0 & 0 \\ 0 & 0 \end{bmatrix} \quad (3.11)$$

The relationship between the measurement vector(Y_{meas}) and the observation matrix(C) is defined by:

$$Y_{meas} = CX \quad (3.12)$$

where:

$$Y_{meas} = [V_L^{GPS} \quad V_L^{WS} \quad \psi_L^{GPS} \quad N_L^{GPS} \quad E_L^{GPS}]^T \quad (3.13)$$

The observation matrix for this model is defined by:

$$C = \begin{bmatrix} 1 & 0 & 0 & 0 & 0 & 0 \\ 1 & 0 & 0 & 0 & 0 & 0 \\ 0 & 0 & 1 & 0 & 0 & 0 \\ 0 & 0 & 0 & 0 & 1 & 0 \\ 0 & 0 & 0 & 0 & 0 & 1 \end{bmatrix} \quad (3.14)$$

The GPS receiver does not directly provide a heading measurement. The measurement from the receiver is course, ν , that is defined as the direction of the velocity vector. Figure 3.7 shows the relation between course, heading, and side slip angle β . Lateral velocity, V_y , is neglected for this thesis, hence β is zero. The course and heading are equal for dynamic scenarios based on this assumption. The course angle is undefined when the UGV is stationary, hence no information on the heading is available. The implications of this assumption are discussed in greater detail in Section 5.3.

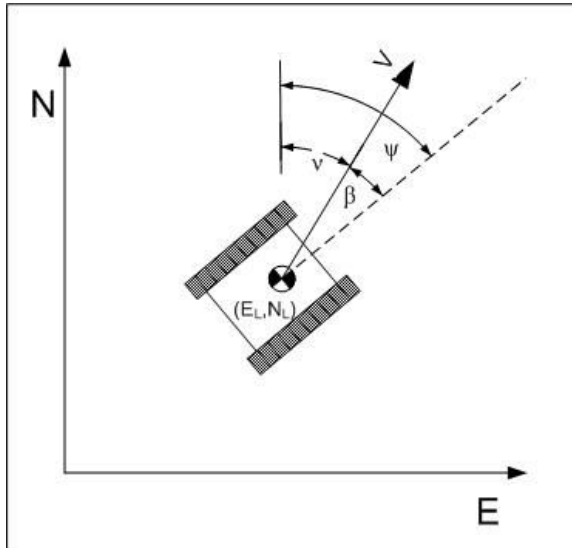


Figure 3.7: Relation of Course (ν), Heading (ψ), and Sideslip (β)

The process noise variances were also assumed to be uncorrelated such that the covariance matrix (Q) is diagonal. The variance of each state is provided in Table 3.1.

Table 3.1: Process Noise Variances

| State | Variance(σ^2) |
|--------|------------------------|
| V_L | 0.00000431 m/s |
| a_b | $10^{-4} m/s^2$ |
| ψ | $10^{-6} deg$ |
| g_b | $10^{-3} deg/s$ |
| N | $10^{-6} m$ |
| E | $10^{-6} m$ |

Additionally, the sensor noises were assumed to be uncorrelated with respect to the other measurements such that the covariance matrix (R) is diagonal. The variance of each measurement is provided in Table 3.2

Table 3.2: Sensor Measurement Noise Variances

| Measured State | Sensor | Variance(σ^2) | Update Rate |
|----------------|---------|------------------------|-------------|
| V_x | GPS | 0.0025 <i>m/s</i> | 4 Hz |
| V_x | Encoder | 0.00000072 <i>m/s</i> | 60 Hz |
| ψ | GPS | 0.000484 <i>deg</i> | 4 Hz |
| N | GPS | 1.832 <i>m</i> | 4 Hz |
| E | GPS | 1.551 <i>m</i> | Hz |

3.3.1 Extended Kalman Filter

The Extended Kalman Filter(EKF) shares many similarities with the standard Kalman Filter. The EKF is used due to the nonlinear dynamics of the model. Unlike the KF which produces an optimal solution, the EKF does not achieve a precisely “optimum” solution due to the linearization process. The solution is “optimal” in the sense that they tend to the optimum [25]. The state equations must be linearized at each time step to ensure that assumptions necessary to employ the EKF are met. The EKF consists of two updates: a time update, and a measurement update. Both updates are implemented at each time step(k). The EKF must also use numerical integration of nonlinear differential equations in the time update.

3.3.2 Measurement Update

The measurement update incorporates the new measurements into the estimator. Ideally only new measurements at that time step are included to prevent corrupting the filter.

The measurement update is defined by:

$$L_k = P_k^- C^T (C P_k^- C^T + R)^{-1} \quad (3.15)$$

$$\hat{X}_k^+ = \hat{X}_k^- + L_k (y_{meas} - C \hat{X}_k^-) \quad (3.16)$$

$$P_k^+ = (I - L_k C) P_k^- \quad (3.17)$$

The \pm notation of the matrices is used to indicate the value with respect to the updates performed at each time step. The notation is used to clarify operations with regards to the measurement and time updates. They are included only for clarification and do not represent an additional operation.

The observation matrix is used to control the measurements that are included in each measurement update. The sensors used by the sensor suite output measurements at 60 Hz and 4 Hz. Table 3.2 from the previous sections shows the update rates for each measurement. Several approaches have been proposed to effectively turn on and off the measurements. One approach is the use of look up tables to select the appropriate C matrix given. This approach requires a separate C matrix to be maintained for each possible combination. An alternate approach was selected in this thesis to use logical operators to switch each entry in the C matrix based on the measurements used for that time step.

3.3.3 Time Update

The time updates propagates the dynamics of the states over each time step(k). The simplest manner is through the use of Euler Integration. A time update using this method is:

$$\hat{X}_{k+1}^- = \hat{X}_k^+ + \Delta t \Phi \quad (3.18)$$

$$P_k^- = \Phi P_k^+ \Phi^T + Q_w \quad (3.19)$$

The Euler Integration provides a very simple operation at the expense of introduction of error. The error stems from the inherent limitation of Euler Integration of functions as time steps are increased. At higher update rates, this limitation is negligible; however, the given 60 Hz measurement update requires a better integration technique.

Runge-Kutta integration can be implemented with a slight increase in computational burden. The time update when implemented with Runge-Kutta integration is:

$$\begin{aligned} K_1 &= \Delta t \dot{X} \\ K_2 &= \Delta t \dot{X} + \frac{K_1}{2} \\ K_3 &= \Delta t \dot{X} + \frac{K_2}{2} \\ K_4 &= \Delta t \dot{X} + \frac{K_3}{2} \\ \hat{X}_{k+1}^- &= \hat{X}_k^+ + \frac{K_1 + 2K_2 + 2K_3 + K_4}{6} \\ M_1 &= \Delta t \left(AP + PA^T + B_w Q B_w^T \right) \end{aligned} \quad (3.20)$$

$$\begin{aligned}
M_2 &= \Delta t \left(A \left(P + \frac{M_1}{2} \right) + \left(P + \frac{M_1}{2} \right) A^T + B_w Q B_w^T \right) \\
M_3 &= \Delta t \left(A \left(P + \frac{M_2}{2} \right) + \left(P + \frac{M_2}{2} \right) A^T + B_w Q B_w^T \right) \\
M_4 &= \Delta t \left(A \left(P + \frac{M_3}{2} \right) + \left(P + \frac{M_3}{2} \right) A^T + B_w Q B_w^T \right) \\
P_k^- &= P_k^+ + \frac{M_1 + 2M_2 + 2M_3 + M_4}{6}
\end{aligned} \tag{3.21}$$

3.3.4 Hybrid Filter

A further improvement on the EKF is a hybrid approach that attempts to overcome some of the difficulties introduced when estimating a continuous process using discrete calculations. The proposed hybrid filter is most appropriate if sampled-data of a continuous process is available. The hybrid filter combines continuous and discrete models in the estimation process. The dynamics, observation and covariance propagation use a continuous model. Discrete models are employed to propagate the measurement update and gain computation [25].

3.3.5 Heading Wrap

An potential issue for implementing the EKF extends from the unique nature of the heading measurement. The heading measurement is usually measured as an angle ranging from 0 to 360 degrees or 0 to 2π radians. The issue arises after one complete revolution of the UGV. Assuming the UGV rotates clockwise, the heading measurement will increase until it reaches 359 degrees. After an additional degree of rotation, the GPS receiver will measure a heading of zero degrees. The estimator will estimate a heading of 360 degrees. The measurements are physically equivalent, but represents an error of 360 degrees.

The problem is further magnified as the UGV completes the second complete rotation. To minimize the effect of this wrap, a subroutine is implemented to unwrap the heading estimate measurement. The routine will add or subtract 360 degrees from the heading to ensure the measurement falls within the appropriate range.

An alternate range for heading was used for this research. The heading is defined over the range of -180 deg to 180 deg or $-\pi$ to π . This alternate definition ensured the estimator encountered both positive and negative residuals. The heading measurements were unwrapped in three separate places within the algorithm. The heading measurements from the GPS receiver were unwrapped to ensure consistency. The heading estimate was also unwrapped for calculation of the measurement update and following the time update. The effect of this operation can be seen in plots of heading as the estimate approaches ± 180 deg. The apparent discontinuity corresponds to a complete revolution of the UGV. The heading measurement can be “rewrapped” if a smooth function is need for analytical analysis.

3.4 Conclusion

An Extended Kalman Filter is employed to receive noisy, incomplete measurements and estimate a systems response. The solution is not by definition optimal; however, the error can be evaluated to ensure proper performance. The EKF provides a relatively simple, yet robust algorithm to estimate the states of the UGV, specifically position, velocity, and heading. The performance of the filter is constrained by the quantity and the quality of the measurements fed into it. When properly implemented, the EKF provides an estimate of

the states shown in Equation (3.6) that is of higher quality than an estimate based on an individual measurement or input.

CHAPTER 4

RELATIVE POSITION MODEL

4.1 Introduction

This chapter develops a relative position estimator, which is an extension of the previously derived navigation estimator. The relative position estimator combines the two navigation estimators with additional measurements utilizing the ultrasonic sensor. The first additional measurement is the range (r) between the center of gravity of two UGVs. The second additional measurement is the bearing (ϕ) between the centerline of the lead UGV and the CG of the trail UGV. The additional measurements provide information on the relative position of both UGVs and the heading of the lead UGV.

4.2 State Transition Matrix

The state transition matrix is comprised of two six state estimators combined into a single twelve state estimator. The same states are maintained, but a designation for lead (l) versus trail (t) UGVs is introduced. The states of the estimator are shown in Equation (4.1).

$$\hat{X} = [\hat{V}_x^l \quad \hat{a}_b^l \quad \hat{\psi}^l \quad \hat{g}_b^l \quad \hat{N}^l \quad \hat{E}^l \quad \hat{V}_x^t \quad \hat{a}_b^t \quad \hat{\psi}^t \quad \hat{g}_b^t \quad \hat{N}^t \quad \hat{E}^t]^T \quad (4.1)$$

The equations governing the states remain the same but are used for each UGV independently. The inclusion of the two relative measurements requires the combination of states

into a single estimator instead of a cascaded approach. This approach incurs a higher computational burden due to inversion of matrices that are twice as large. A cascaded approach based on the use of two navigation estimators feeding a third estimator to include the relative measurements would minimize the effect of the relative measurements while complicating the implementation. Use of the estimates from the navigation estimators as measurements for the third estimator could introduce correlated noise, thus corrupting the output. The application could provide comparable or improved results; however, this approach would require significantly more analysis to evaluate the process noise of all three estimators. The nonlinear state equations must be evaluated and linearized, as before, at each time step. The Jacobian of the state matrix is shown in Equation (4.2).

$$J_A = \begin{bmatrix} 0 & -1 & 0 & 0 & 0 & 0 & 0 & 0 & 0 & 0 & 0 & 0 \\ 0 & 0 & 0 & 0 & 0 & 0 & 0 & 0 & 0 & 0 & 0 & 0 \\ 0 & 0 & 0 & -1 & 0 & 0 & 0 & 0 & 0 & 0 & 0 & 0 \\ 0 & 0 & 0 & 0 & 0 & 0 & 0 & 0 & 0 & 0 & 0 & 0 \\ \cos(\psi) & 0 & -V_L \sin(\psi) & 0 & 0 & 0 & 0 & 0 & 0 & 0 & 0 & 0 \\ \sin(\psi) & 0 & V_L \cos(\psi) & 0 & 0 & 0 & 0 & 0 & 0 & 0 & 0 & 0 \\ 0 & 0 & 0 & 0 & 0 & 0 & 0 & -1 & 0 & 0 & 0 & 0 \\ 0 & 0 & 0 & 0 & 0 & 0 & 0 & 0 & 0 & 0 & 0 & 0 \\ 0 & 0 & 0 & 0 & 0 & 0 & 0 & 0 & 0 & -1 & 0 & 0 \\ 0 & 0 & 0 & 0 & 0 & 0 & 0 & 0 & 0 & 0 & 0 & 0 \\ 0 & 0 & 0 & 0 & 0 & 0 & \cos(\psi) & 0 & -V_L \sin(\psi) & 0 & 0 & 0 \\ 0 & 0 & 0 & 0 & 0 & 0 & \sin(\psi) & 0 & V_L \cos(\psi) & 0 & 0 & 0 \end{bmatrix} \quad (4.2)$$

4.3 Inputs

The inputs for the system are the accelerometer and rate gyro measurements provided by the sensor suites on each UGV. The noise characteristics for the lead and trail IMU are unique and are accounted for in the Q matrix. The inputs from each UGV will be comparable given identical system dynamics. The inputs to the estimator are defined in Equation (4.3).

$$u = [a_{long}^l \quad r_z^l \quad a_{long}^t \quad r_z^t]^T \quad (4.3)$$

4.4 Input Matrix

The dimensions of the input matrix are increased in the same manner as the dimensions of the state matrix. Two sets of acceleration and rotation measurements comprise the inputs to the system. The acceleration and rotation measurements are fed directly into the velocity

and heading states, respectively. The resulting matrix is

$$B = \begin{bmatrix} 1 & 0 & 0 & 0 \\ 0 & 0 & 0 & 0 \\ 0 & 1 & 0 & 0 \\ 0 & 0 & 0 & 0 \\ 0 & 0 & 0 & 0 \\ 0 & 0 & 0 & 0 \\ 0 & 0 & 1 & 0 \\ 0 & 0 & 0 & 0 \\ 0 & 0 & 0 & 1 \\ 0 & 0 & 0 & 0 \\ 0 & 0 & 0 & 0 \\ 0 & 0 & 0 & 0 \end{bmatrix} \quad (4.4)$$

4.5 Measurements

The relative position estimator uses the same measurements as the navigation estimator plus measurements from the ultrasonic sensor. The measurements used by the estimator are shown in Equation (4.5).

The notation for Equation (4.5) separates the global measurements for each UGV and the relative measurements between them. The first ten measurements use the global ENU reference frame. The last two measurements are relative measurements in the lead UGV body fixed frame. A subscript is added to the relative measurements to clarify the reference

used to provide the measurement.

$$\begin{aligned}
Y_l &= [V_l^{GPS} \quad V_l^{WS} \quad \psi_l^{GPS} \quad N_l^{GPS} \quad E_l^{GPS}] \\
Y_t &= [V_t^{GPS} \quad V_t^{WS} \quad \psi_t^{GPS} \quad N_t^{GPS} \quad E_t^{GPS}] \\
Y_{rel} &= [r_{lt} \quad \phi_{lt}] \\
Y_{meas} &= [Y_l \quad Y_t \quad Y_{rel}]^T
\end{aligned} \tag{4.5}$$

Figure 4.1 shows the relation of the bearing and range to the positions of the UGVs. The measurements provided by the ultrasonic sensor must be transformed into the global coordinate frame for use by the EKF. These measurements provide additional information about the relative position of both UGVs and the orientation of the lead UGV. A third bearing measurement in the trail UGV body fixed frame would be required to gain additional information about the orientation of that UGV.

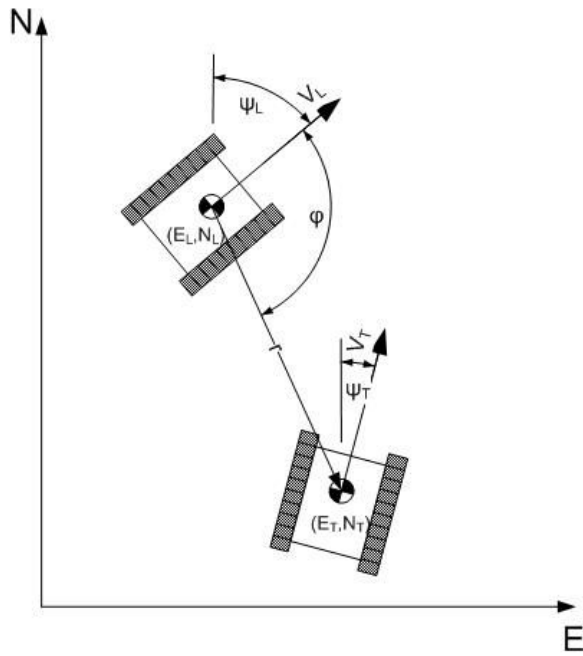


Figure 4.1: Description of Range and Bearing Measurement

The range measurement used by the estimator is defined by Equation (4.6).

$$r = \sqrt{(E^{trail} - E^{lead})^2 + (N^{trail} - N^{lead})^2} \quad (4.6)$$

The bearing measurement requires a transformation from the body fixed frame of the lead UGV to the global reference frame. Figure 4.2 illustrates the relationship between the relative bearing measurement and the global heading of the UGV.

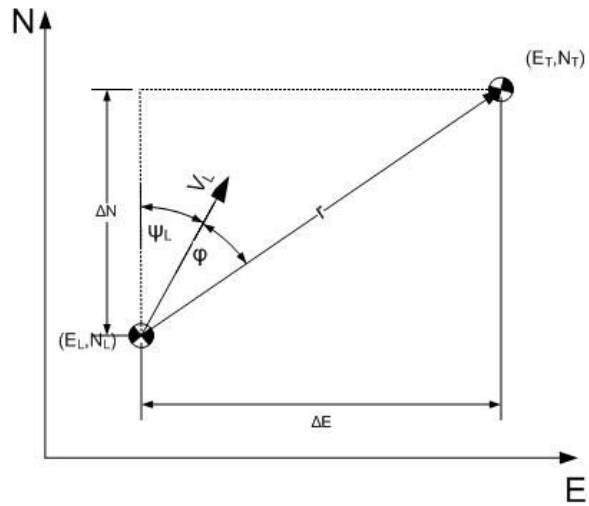


Figure 4.2: Derivation of Bearing Measurement

The equation that defines the bearing measurement is:

$$\phi = \text{atan} \frac{\Delta E}{\Delta N} - \psi_l \quad (4.7)$$

4.6 Observation Matrix

The estimator uses a 12 x 12 observation matrix to relate the measurements to the states. The first 10 rows are created by using the observation matrix from the navigation estimator used in Chapter 3. The last two rows are derived from Equations (4.6) and (4.7). The matrix must be linearized and evaluated at each time step along the estimator's nominal trajectory using the Jacobian. The Jacobian of the observation matrix is defined by

$$J_C = \begin{bmatrix} \frac{\partial f_1}{\partial x_1} & \dots & \frac{\partial f_1}{\partial x_n} \\ \vdots & \ddots & \vdots \\ \frac{\partial f_n}{\partial x_1} & \dots & \frac{\partial f_n}{\partial x_n} \end{bmatrix} \quad (4.8)$$

This results in the following Jacobian observation matrix:

$$J_C = \begin{bmatrix} 1 & 0 & 0 & 0 & 0 & 0 & 0 & 0 & 0 & 0 & 0 & 0 \\ 1 & 0 & 0 & 0 & 0 & 0 & 0 & 0 & 0 & 0 & 0 & 0 \\ 0 & 0 & 1 & 0 & 0 & 0 & 0 & 0 & 0 & 0 & 0 & 0 \\ 0 & 0 & 0 & 0 & 1 & 0 & 0 & 0 & 0 & 0 & 0 & 0 \\ 0 & 0 & 0 & 0 & 0 & 1 & 0 & 0 & 0 & 0 & 0 & 0 \\ 0 & 0 & 0 & 0 & 0 & 0 & 1 & 0 & 0 & 0 & 0 & 0 \\ 0 & 0 & 0 & 0 & 0 & 0 & 1 & 0 & 0 & 0 & 0 & 0 \\ 0 & 0 & 0 & 0 & 0 & 0 & 0 & 0 & 1 & 0 & 0 & 0 \\ 0 & 0 & 0 & 0 & 0 & 0 & 0 & 0 & 0 & 0 & 1 & 0 \\ 0 & 0 & 0 & 0 & 0 & 0 & 0 & 0 & 0 & 0 & 0 & 1 \\ 0 & 0 & 0 & 0 & \frac{-\Delta N}{\sqrt{\Delta N^2 + \Delta E^2}} & \frac{-\Delta E}{\sqrt{\Delta N^2 + \Delta E^2}} & 0 & 0 & 0 & 0 & \frac{\Delta N}{\sqrt{\Delta N^2 + \Delta E^2}} & \frac{\Delta E}{\sqrt{\Delta N^2 + \Delta E^2}} \\ 0 & 0 & -1 & 0 & \frac{\Delta E}{\Delta N^2 + \Delta E^2} & \frac{-\Delta N}{\Delta N^2 + \Delta E^2} & 0 & 0 & 0 & 0 & \frac{-\Delta E}{\Delta N^2 + \Delta E^2} & \frac{\Delta N}{\Delta N^2 + \Delta E^2} \end{bmatrix} \quad (4.9)$$

4.7 Extended Kalman Filter

The relative position estimator uses the same measurement and time updates as described in Section 3.3.1. The dimensions of the matrices that are evaluated for the updates are twice as large, but handled in the same manner. The inclusion of the relative measurements requires evaluation of the Jacobian of the observation matrix (C), shown in Equation

(4.9), at each time step. The process noise covariance matrix (Q) and the measurement noise covariance matrix (R) are populated with the empirically determined values for the corresponding measurement or input.

4.8 Conclusion

This Chapter has provided the state matrices used to design the relative navigation estimator used in this thesis. The use of a common time allows ultrasonic sensors to reliably measure relative range and bearing between the two UGVs. These two additional measurements provide valuable information that allows the EKF to refine the position and heading estimates. This approach builds on the navigation estimator derived in Chapter 3. An increased computational burden is incurred to implement the estimator due to the increased number of states. The ultrasonic sensors are the only additional hardware required to implement this estimator. The marked improvement in the state estimates provided by the inclusion of the relative measurements offset the additional computational costs. The additional hardware does not significantly affect system cost or degrade payload capability. Chapter 5 will provide the design of the relative navigation estimator as well as experimental validation of the algorithm.

CHAPTER 5
EXPERIMENTAL WORK

5.1 Introduction

This Chapter presents the experimental results of tests performed on the individual sensors and the system as a whole. The measured noise characteristics for each sensor used to instrument the UGV are presented. Simulated data is used to evaluate and compare the navigation estimator and the relative position estimator. These results were used to verify proper operation and provide insight into the level of performance that could be expected based on the empirically determined noise characteristics. Experimental results are presented to demonstrate the EKF's performance with measurements taken under normal operating conditions. The experimental results are also used to validate the simulated results.

5.2 Sensor Data

The EKF uses the process noise covariance matrix (Q) to weight each measurements contribution. The sensor noises are assumed to be additive white noise with Gaussian distribution. The variance is the metric used to quantify the noise by the EKF. Each sensor is commercially available with statistical values provided in the specification sheets. These values are important since the quality of the estimate provided by the EKF is a function of the quality of the measurements and how well the noise can be modeled.

5.2.1 IMU

The Sentera IMU was tested over three separate ten minute periods to determine the mean and standard deviation for each accelerometer and gyro. This approach provides a sample size that is comparable to the measurements taken in an experimental run. The separate data sets also provide insight into the health of the sensors and the presence of other error sources such as drift or bias walk. A significant increase in noise or a drifting mean value is an indicator of MEMS failure.

Accelerometer

The parameters determined from averaging the three runs closely match the performance specs provided by Sentera shown in Table 2.3. Tables 5.1 and 5.2 provide the measured standard deviations and means for the accelerometers on both IMUs. The EKF should calculate a bias that is comparable to the mean value for each sensor. Platform dynamics will cause the EKF estimate to vary; however, the values should be very close under steady state conditions.

Table 5.1: Lead Accelerometer Noise

| Parameter | Value (m/s^2) |
|------------|-------------------|
| σ_x | 0.0042 |
| $bias_x$ | -0.01443 |
| σ_y | 0.0002893 |
| $bias_y$ | -0.02221 |
| σ_z | 0.0002954 |
| $bias_z$ | -0.0003018 |

Table 5.2: Trail Accelerometer Noise

| Parameter | Value (m/s^2) |
|------------|-------------------|
| σ_x | 0.01116 |
| $bias_x$ | -0.01380 |
| σ_y | 0.01189 |
| $bias_y$ | -0.03640 |
| σ_z | 0.01802 |
| $bias_z$ | 0.003535 |

Rate Gyroscope

The parameters calculated for the rate gyroscopes are shown in Tables 5.3 and 5.4. These values are higher than the specifications shown in Table 2.3 but fall within the expected range for a MEMS based gyro. The slightly higher values of the trail IMU are due to the use of earlier model Analog Digital rate gyros. These values can provide reasonable performance for dead reckoning for several seconds. The EKF receives GPS updates at 4 Hz, which bounds the heading estimate error to acceptable levels.

Table 5.3: Lead Gyro Noise

| Parameter | Value (<i>deg/s</i>) |
|------------|------------------------|
| σ_x | 0.3916 |
| $bias_x$ | -0.1877 |
| σ_y | 0.4310 |
| $bias_y$ | -0.3883 |
| σ_z | 0.4161 |
| $bias_z$ | -0.0983 |

Table 5.4: Trail Gyro Noise

| Parameter | Value (<i>deg/s</i>) |
|------------|------------------------|
| σ_x | 1.4090 |
| $bias_x$ | 0.04732 |
| σ_y | 1.4962 |
| $bias_y$ | -0.1014 |
| σ_z | 1.8112 |
| $bias_z$ | -0.1854 |

5.2.2 GPS

The noise measurements for the GPS receivers are presented in Table 5.5 and 5.6. These parameters provide an indication of the quality of the measurement calculated by the receiver, but they do not completely describe the noise present. The error present in the measurements is “colored” in that it does not exhibit precisely zero mean white noise. The position measurements exhibit “walk” over time. The measured position follows

a meandering path that is centered about a central point. Figure 3.1 shown previously illustrates this walk that is common to all GPS receivers regardless of cost.

Table 5.5: Lead GPS Noise

| Parameter | Value (m) |
|------------|---------------|
| σ_N | 1.8320 |
| σ_E | 1.5551 |

Table 5.6: Trail GPS Noise

| Parameter | Value (m) |
|------------|---------------|
| σ_N | 1.6651 |
| σ_E | 1.9698 |

5.2.3 Ultrasonic Sensor

The Ping sensors are capable of providing reliable measurements under static and dynamic testing. Static test sessions were implemented to calculate the parameters necessary to accurately describe the range and bearing noise. The range and bearing measurements were produced by the returns of the sensors located on the lead UGV. Figure 5.1 illustrates the relationship between the raw range measurements, r_l and r_r , and the measurements used for estimation, r and ϕ .

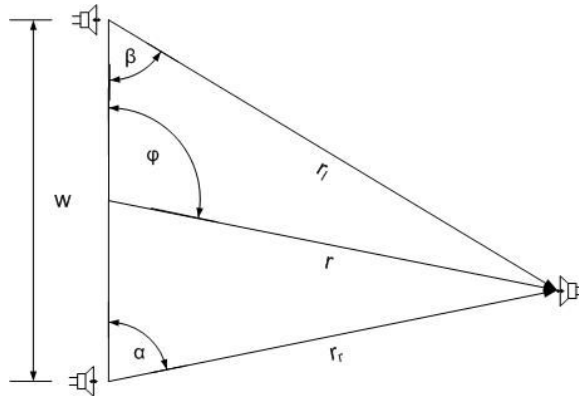


Figure 5.1: Schematic Illustrating the Range and Bearing Calculation

The range and bearing measurements are defined by Equations (5.1-5.3).

$$\beta = \text{acos} \left(\frac{r_l^2 + w^2 - r_r^2}{2r_l w} \right) \quad (5.1)$$

$$r = \sqrt{\frac{r_l^2 + w^2}{4} - r_l w \cos(\beta)} \quad (5.2)$$

$$\phi = \text{acos} \left(\frac{r^2 + \frac{w^2}{4} - r_l^2}{r w} \right) \quad (5.3)$$

The measurements from the Ping sensor are quite precise when using the GPS PPS to provide a common time for the sensor suites. Errors introduced are based on variances of the PPS signal and delays due to computations of the RCM4100. Variations in temperature will induce a bias since the measurements are based off of time of flight. A ten minute sample of static range and bearing measurements are shown in Figure 5.2 and Figure 5.3 respectively. The actual range measured for the test was 2.431 m. The actual bearing between units for the test was 90 deg.

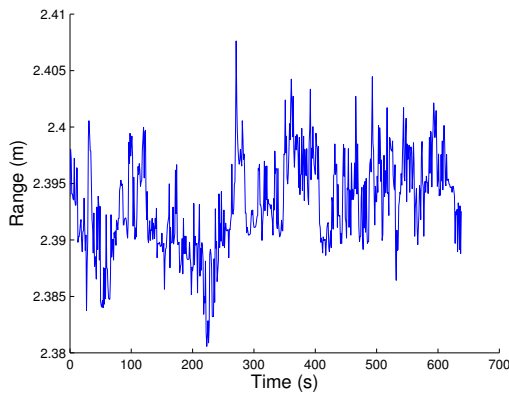


Figure 5.2: Experimental Ultrasonic Range Measurements

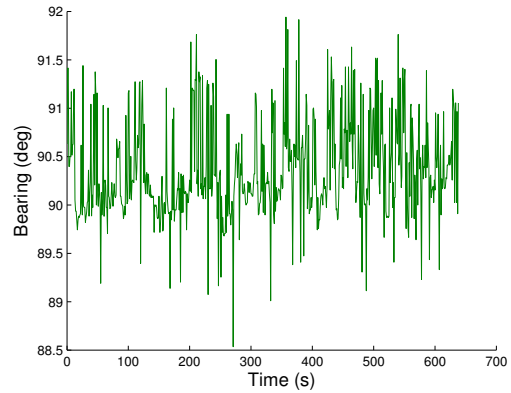


Figure 5.3: Experimental Ultrasonic Bearing Measurements

The statistics characterizing the error present in the measurements are listed in Table 5.7. The precision of the ultrasonic measurements are offset by their 1Hz rate. An avenue for additional work would focus on increasing the frequency of the measurements.

Table 5.7: Ultrasonic Sensor Noise

| Parameter | Value |
|--------------------|------------|
| $mean_{range}$ | 0.038 m |
| σ_{range} | 0.004163 m |
| $mean_{bearing}$ | 0.036 deg |
| $\sigma_{bearing}$ | 0.5064 deg |

5.3 Navigation Estimator

The navigation estimator employs a relatively simple routine to estimate the six states identified in Chapter 3. The estimator provides reliable results given a valid model and accurate noise statistics. However, an error in either the model or the noise statistics can yield unreliable estimates or an unstable estimator. The observability of the system was verified to ensure that all states could be estimated from the measurements. The stability of the estimator was also verified to ensure proper operation.

5.3.1 Simulated Static Data

A set of simulated measurements was produced to replicate measurements from a stationary UGV. The simulated measurements include a zero mean normal distribution scaled to approximate the standard deviation of the respective sensor noise. Figure 5.4 compares the GPS position measurements to the EKF's position estimates. The initial measurement

is used to initialize the EKF, which is the position of the initial outlier. The filter refines its estimate as additional measurements are available.

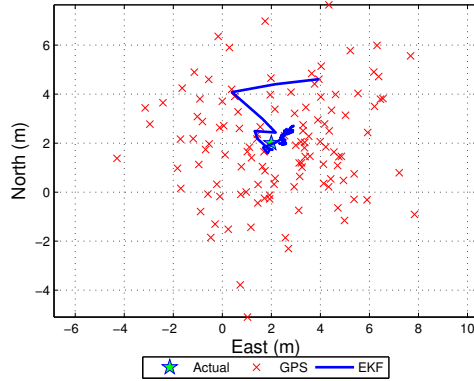


Figure 5.4: Simulated Static Position Estimate

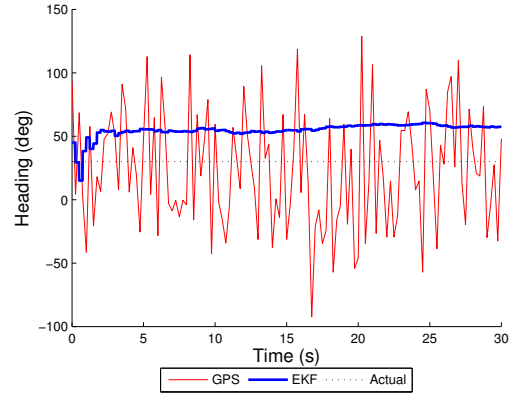


Figure 5.5: Simulated Static Heading Estimate

Figure 5.5 illustrates the inability of the EKF to estimate heading when stationary. The heading obtained from GPS is discarded to prevent corruption of the estimate with the introduction of false readings. The GPS receiver is unable to measure a course as discussed previously in Section 3.2.1. GPS from a single antennae cannot provide a deterministic measure of heading when the vehicle is stationary. The noise present in the heading measurement is a function of the measured velocity. Equation (5.4) is used to model the inverse relationship between the noise and velocity [8].

$$\sigma_{\psi}^{GPS} = \frac{\sigma_V^{GPS}}{V_{GPS}} \quad (5.4)$$

In this research, the heading measurements provided by the GPS receiver were discarded when the UGV’s velocity fell below 0.1 m/s. Below this threshold the noise represents the largest component of the measurement. When the heading measurement is discarded the EKF integrates only the rate gyro input with each time update. The heading estimate is allowed to “coast” based on the IMU inputs until the next heading measurement is available.

The performance of the filter when estimating a static position is shown in Figure 5.6. The position error drops to within 30 cm during the 30 second run. The mean of the error after the filter settled is 0.5787 m with a standard deviation of 0.2083 m. The first two seconds worth of estimates are discarded when calculating statistics due to the presence of transient error. This mean value and standard deviation provides a significant improvement over a GPS only estimate. Figure 5.7 shows the EKF’s heading estimate over the same period. The heading error is a function of the values used to initialize the filter and the noise present in the rate gyro inputs. The estimate does not provide any useful information with regards to the heading of the UGV.

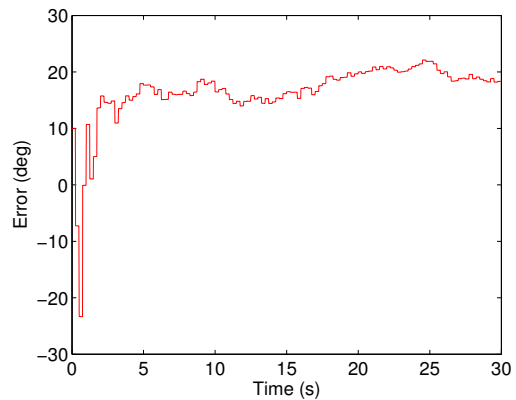
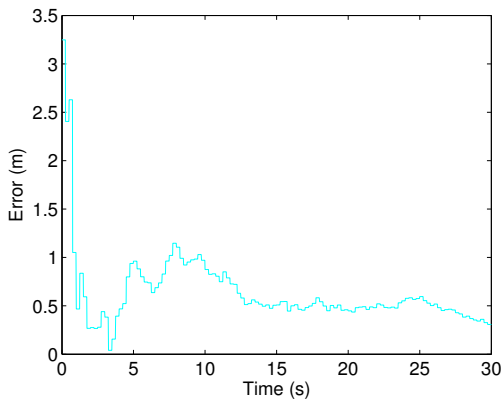


Figure 5.6: Simulated Static Position Error

Figure 5.7: Simulated Static Heading Error

5.3.2 Simulated Dynamic Data

A second set of test data is used to simulate the UGV accelerating from zero velocity to a constant velocity. The heading is held constant to evaluate the performance of the filter in estimating a heading with available GPS measurements during non stationary tests. Noise was incorporated representative of the noise present in the actual measurements. Figure 5.8 demonstrates the EKF's ability to accurately estimate the position. Figure 5.9 shows that the inclusion of heading measurements does allow the filter to provide an accurate estimate of heading.

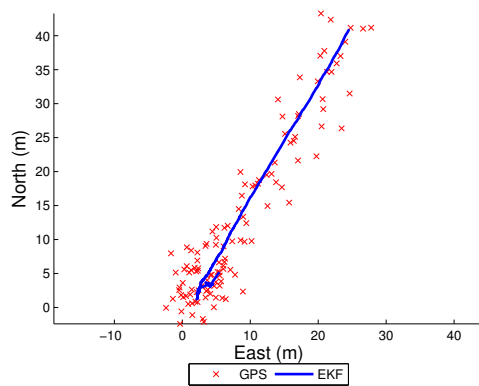


Figure 5.8: Simulated Linear Position Estimate

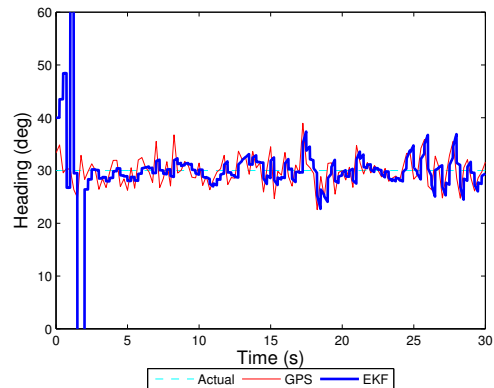


Figure 5.9: Simulated Linear Heading Estimate

The EKF provides a reasonably accurate position estimate with an average error of 0.25 m and standard deviation of 0.1412 m. The heading estimate has an average error of -0.214 degrees and a standard deviation of 1.6818 degrees. These statistics were calculated after the filter settled at three seconds.

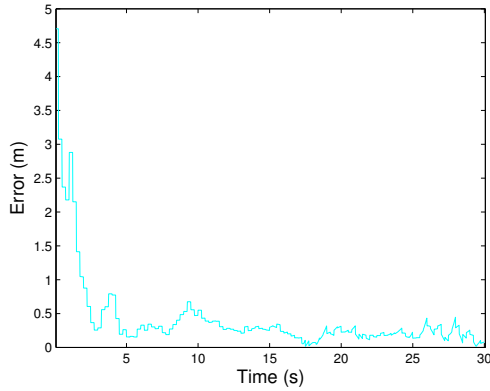


Figure 5.10: Simulated Linear Position Error

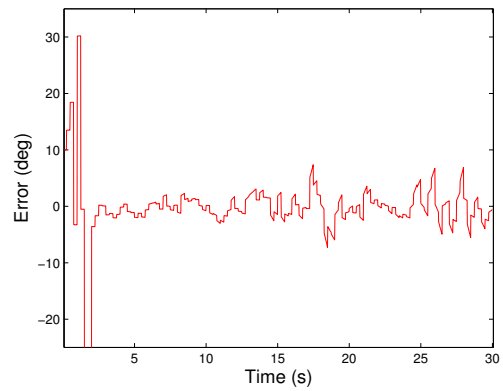


Figure 5.11: Simulated Linear Heading Error

A second set of simulated dynamic inputs and measurements were generated to validate the EKF at a constant speed with varying yaw rates. A square path with rounded corners simulated the path of the UGV while it maintained a constant velocity. This path closely matches conditions the UGV would likely see during operation. Figure 5.12 shows the simulated path with the GPS coordinates overlaid for reference and the estimate from the EKF. The filter is initialized with the first position measurement, and as a result requires time to provide an accurate estimate. The EKF was able to estimate the UGVs position to within 20 cm by the end of the 30 second run. The mean position error was 0.3409 m with a standard deviation of 0.1411 m. The mean error is slightly higher than the error present in the straight line simulation; however, the standard deviation is comparable. Figure 5.13 compares the heading estimate to the actual heading over the entire course. The EKF successfully estimates heading when receiving GPS heading measurements. This bounds the error from the integration of the inputs due to noise and drift in the gyro. The mean heading error for the run is -1.085 deg with a standard deviation of 8.49 degrees. These values are significantly higher than those present in the straight line simulation. The

increase can be attributed to the inclusion of the four turns coupled with the noisy rate gyro and heading measurements.

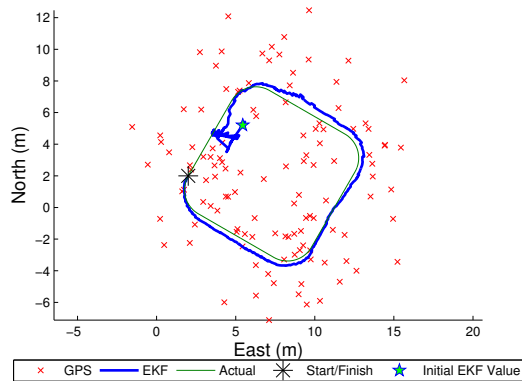


Figure 5.12: Simulated Square Position Estimate

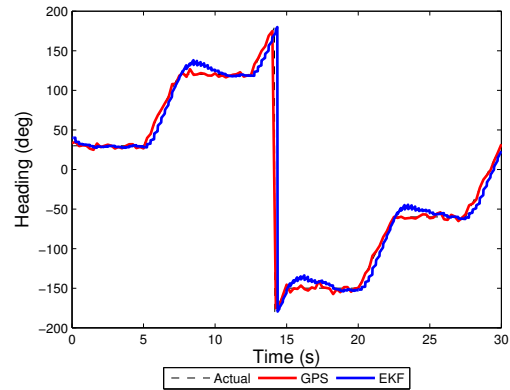


Figure 5.13: Simulated Square Heading Estimate

The final set of simulated inputs changed yaw rate and acceleration sinusoidally. The scenario simulates the UGV following a series of tight serpentine turns or chicane while accelerating. This scenario was evaluated to ensure the filter was robust and to prevent problems later when evaluating experimental data. Figure 5.14 compares the EKF estimate to the simulated path. The velocity in this simulation is significantly greater than the maximum speed of the MATILDA, but the scenario does provide confidence in the capabilities of the filter. Figure 5.15 compares the heading estimate to the actual heading. The filter is able to provide a reliable estimate even with change in speed and heading. The EKF's performance using simulated data provides confidence in the ability to estimate the states using actual measurements.

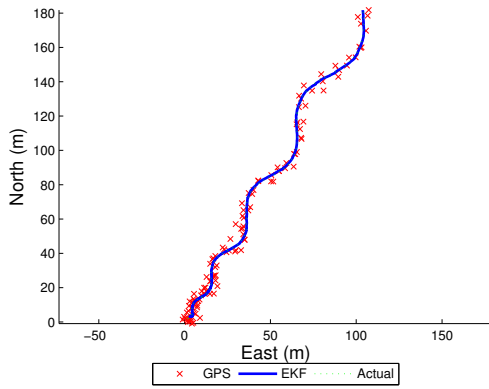


Figure 5.14: Simulated Chicane Position Estimate

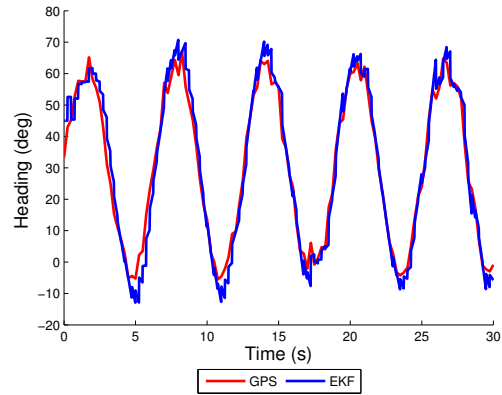


Figure 5.15: Simulated Chicane Heading Estimate

5.3.3 Experimental Performance

The EKF was then evaluated using actual measurements received from both sensor suites. Data from the same time period was used for both sensor suites to save time testing and also to ensure the use of the same GPS satellites. Ideally, the receivers should provide measurements with similar dilutions of precision (DOP) when using the same satellite signals. The separate runs provided an opportunity to identify any anomalies in the measurements.

Static Experimental Data

In this experiment, the test rigs were spaced 2.413 m apart while mounted on the UGV to provide as realistic performance as possible. The two units were arrayed along the same Easting with the lead unit being the southern unit. The orientation was selected to ease comparison of position and heading data. The measurements from these runs were used to

calculate the noise of each sensor. The position and heading estimates for the lead unit are shown in Figure 5.16. The estimates for the trail unit are provided in Figure 5.17.

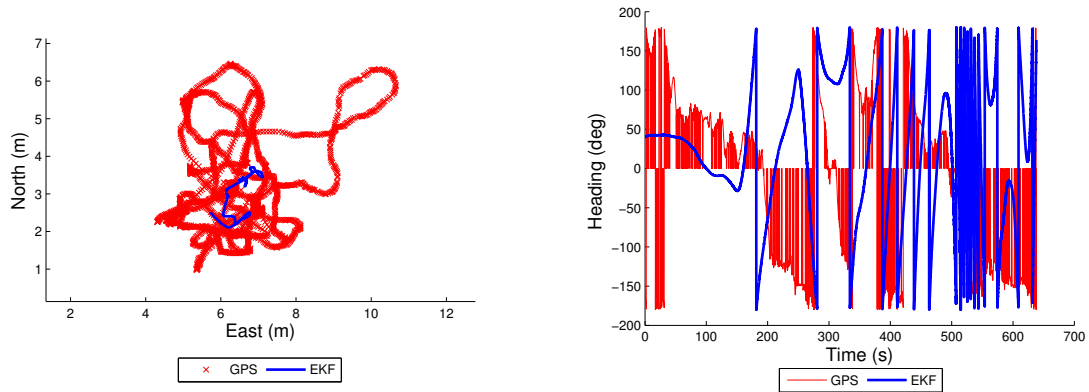


Figure 5.16: Experimental Lead Unit Static Estimate

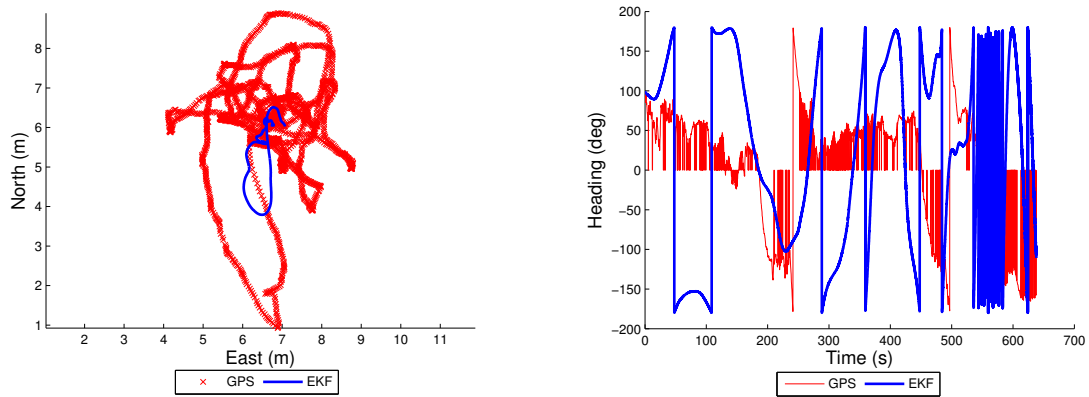


Figure 5.17: Experimental Trail Unit Static Estimate

The results using the experimental data are comparable to the simulated runs. The heading estimate suffers due to lack of heading measurements as was seen in the simulated data experiments. The integration of the input from the rate gyro yields an estimate; however, the effect of noise and drift is seen over time. A comparison of the standard deviation of the simulated and experimental position estimates are provided in Table 5.8.

The values closely match between the simulated and experimental data. The simulated data used additive white noise to simulate the noise present in the measurements. The noise present in the experimental measurements include limited frequency content. The slight variation in the values for the experimental data is due to the “color” of the noise present in the actual measurements.

Table 5.8: Simulated and Experimental Position Standard Deviation

| | σ_N | σ_E |
|--------------------|-----------------|-----------------|
| Simulated | 0.4197 <i>m</i> | 0.3507 <i>m</i> |
| Experimental Lead | 0.434 <i>m</i> | 0.2659 <i>m</i> |
| Experimental Trail | 0.6249 <i>m</i> | 0.2069 <i>m</i> |

Dynamic Experimental Data

The first dynamic scenario involved driving the UGV in a straight line at a constant speed from north to south. A MATILDA carried a sensor suite and towed a second sensor suite 2.431 meters behind along the same path. The same speed was maintained with a brief pause in the middle of the run. The estimate initially diverged due to faulty heading readings from the GPS receivers. The receiver heading measurements were correct after several seconds and the estimates began to converge. No information was exchanged between the sensor suites for these estimates. Figure 5.18 shows the performance of the estimator using data from the lead UGV. The measurements and position estimate for the EFK using data from the trail UGV is shown in Figure 5.19. The scale of the East axis is exaggerated to show detail. If presented with axis of equal scale the position estimate appears as a straight line.

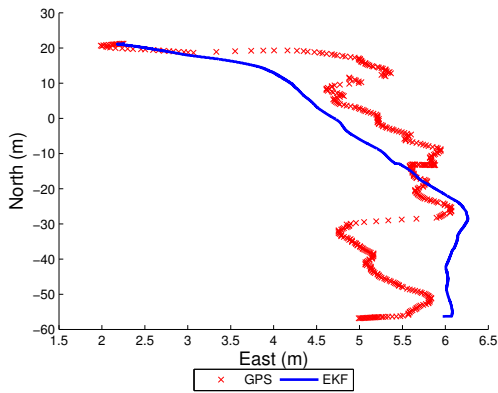


Figure 5.18: Line Lead Position Estimate

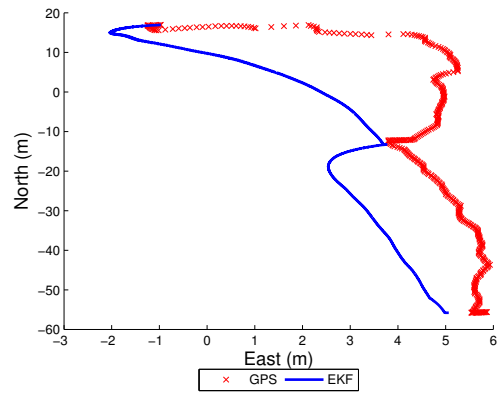


Figure 5.19: Line Trail Position Estimate

The heading estimate provided by the EKF is significantly improved when heading measurements are available. The heading estimate for the lead UGV is shown in Figure 5.20. The MATILDA paused in the middle of the run causing faulty GPS readings for the trail unit. The heading estimate suffers as a result as seen in Figure 5.21 at 60 seconds. The position estimate for the trail unit at this point also suffers due to the heading error as the position estimate laterally diverges.

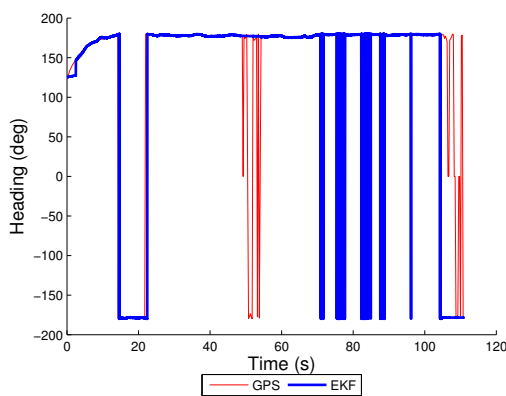


Figure 5.20: Line Lead Heading Estimate

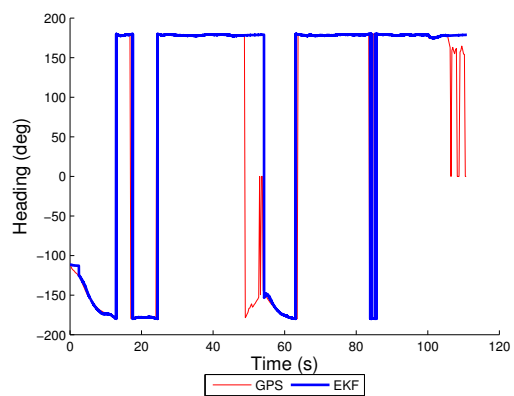


Figure 5.21: Line Trail Heading Estimate

The second dynamic scenario was performed by driving the UGV in an elliptical path. Fine steering adjustments of the MATILDA are difficult if not impossible in its current form. Therefore a smooth trajectory was selected due to its ease of replication and ability to achieve the desired path. The smooth trajectory also ensures the sensor suites followed the same path. The separation between the units was reduced to 1.34 m due to the size of the test area. Figure 5.22 shows the position estimate using data from the lead UGV. A similar result shown in Figure 5.23 shows how varying measurements yield different estimates given identical paths. The estimator was able to approximate the path driven despite GPS measurements that were skewed due to multipath.

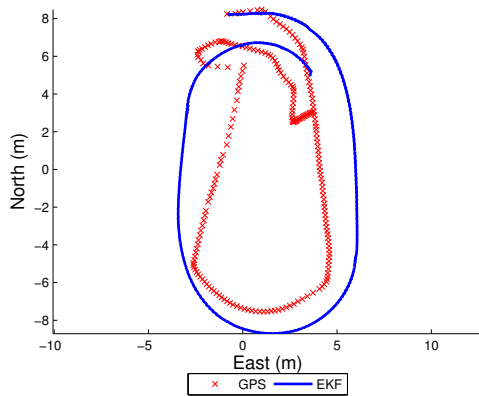


Figure 5.22: Elliptical Lead Position Estimate

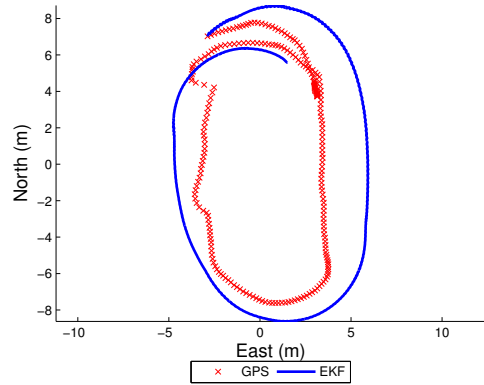


Figure 5.23: Elliptical Trail Position Estimate

Figure 5.24 presents the heading estimate from the EKF using data from the lead UGV. As with the straight line experiments, the EKF is able to accurately estimate heading when GPS measurements are included to bound the error introduced by the integration of IMU input noise. The heading estimate for the trail UGV is shown in Figure 5.25. The EKF provides reasonable estimates from the data provided by both sensor suites. The estimates

vary slightly due to the noise inherent to the process and measurements from each set of sensors.

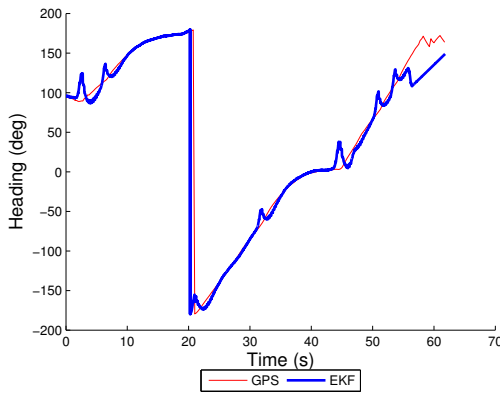


Figure 5.24: Lead Heading Estimate

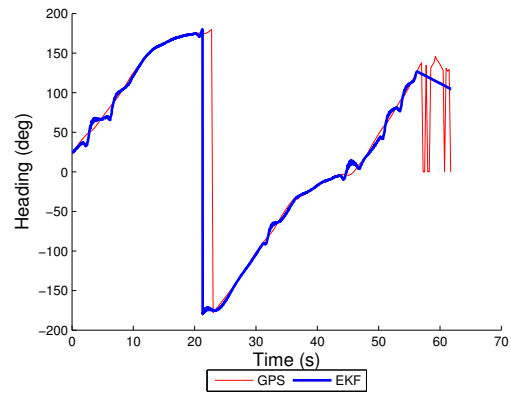


Figure 5.25: Trail Heading Estimate

5.4 Relative Position Estimator

The relative position estimator was evaluated in the same manner as the navigation estimator to evaluate the limit of its performance. The same simulated data is used from the previous section for the lead UGV. A second set simulated data is used for the trail UGV to ensure no correlation in the noise of the measurements.

5.4.1 Simulated Static Lead with Static Trail

The first scenario evaluated the relative position estimator using stationary UGVs. The lead UGV was placed at three meters north and four meters east with an initial heading of 45 degrees. The trail UGV was placed at three meters north and twelve meters north with an initial heading of 45 degrees. This results in a bearing from the lead UGV to the trail

UGV of 45 degrees. The EKF is fed 30 seconds of simulated measurement to evaluate its performance.

This estimator improves the trail position estimate when compared to the results from the navigation estimator developed in Chapter 3. The relative position estimator uses global information on both UGVs and relative information on the position and orientation to generate the estimates. The trail position improvement is due to the inclusion of the range measurement. Two coordinates are necessary to define a point in a plane. In this case, the range confines the trail position to an arc about the lead position with a radius equal to the range measurement. The position estimate for the lead UGV is significantly improved due the combination of the range and heading measurement. These relative polar coordinates define the lead position given a trail position. Figure 5.26 demonstrates the effect of the additional measurement. Figure 5.27 compares the position error of the lead and trail UGV. The lead position is visibly improved over the trail position without degrading the trail position.

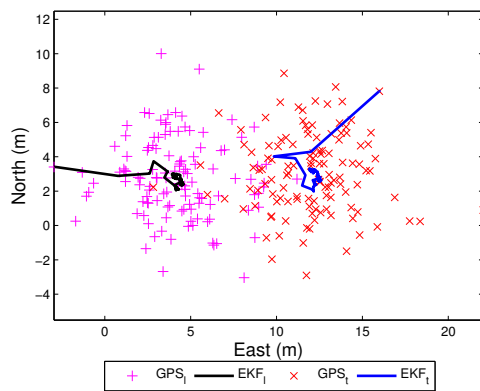


Figure 5.26: Simulated Static Position Estimate

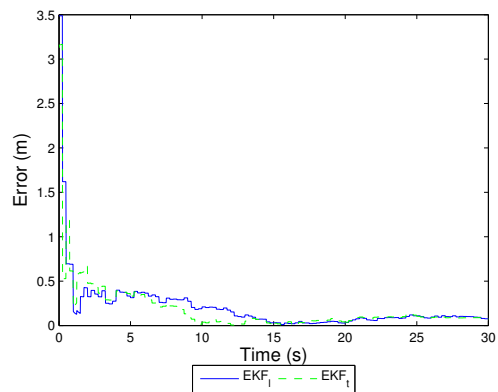


Figure 5.27: Simulated Static Position Error

The average errors and the standard deviation of the error is presented in Table 5.9. The error characteristics from the navigation estimates are included for comparison. The estimators used identical inputs and measurements for the navigation estimator and the lead unit for the relative position estimator. A comparison of these values further demonstrates gains realized through the inclusion of the relative measurements.

Table 5.9: Simulated Static Position Estimate Error and Standard Deviation

| | <i>mean</i> | σ |
|--------------------------|-----------------|-----------------|
| Navigation Estimator | 0.5787 <i>m</i> | 0.2083 <i>m</i> |
| Relative Estimator Lead | 0.183 <i>m</i> | 0.108 <i>m</i> |
| Relative Estimator Trail | 0.1482 <i>m</i> | 0.0575 <i>m</i> |

The heading estimate for the lead UGV quickly converges to zero as seen in Figure 5.28. This appears to be the result of an error within the algorithm, but upon further investigation represents the appropriate solution. When the UGV is stationary no heading measurements are available. The GPS heading measurements are presented in the plots for reference only. As a result, the EKF has no measurements to bound the error incurred by the noise introduced by the rate gyro. The heading estimate for the trail UGV shows how the estimate drifts over time due to this error. The bearing measurement requires transformation from the body fixed frame to the global ENU frame, thus the heading state for the lead UGV is related to the relative bearing measurement. The EKF minimizes the error of each state with the corresponding measurements. The EKF minimizes the error associated with the bearing measurement by driving the lead heading estimate to zero. With no heading measurements, the EKF has no basis for comparison to the actual heading of the UGV. Figure 5.29 compares the estimates to the true heading, further demonstrating

the point. The lead UGV estimate is not accurate, but does provide information on the relative orientation of the UGVs.

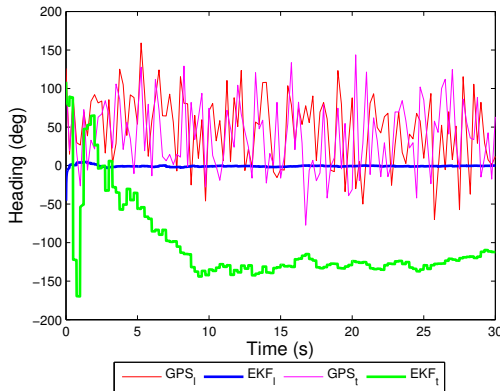


Figure 5.28: Simulated Static Heading Estimate

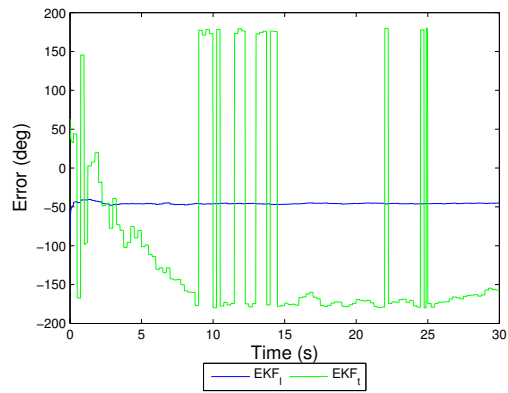


Figure 5.29: Simulated StaticHeading Error

This simulation was also used to tune the filter and ensure the additional measurements will yield improved estimates. The initial values used for the process noise covariance matrix actually produced estimates with more error than the navigation estimator. Inspection of the Kalman Gain (L) showed the bearing measurement was improperly weighted. The faulty weight corrupted the lead heading measurement and subsequently the position estimate for the lead UGV. More appropriate values for the process noise covariance matrix were selected and the additional simulated runs generated the expected improvements. The final process noise and measurement noise covariance matrices are provided in Table 5.10 and Table 5.11 respectively.

Table 5.10: Process Noise Covariance

| Position | Parameter | Value |
|-------------|---------------------------------|-----------------------------|
| $Q_{1,1}$ | $\sigma_{ax}^2 \times \Delta T$ | 4.3121e-6 <i>m/s</i> |
| $Q_{2,2}$ | ax_{walk} | 0.01 <i>m/s²</i> |
| $Q_{3,3}$ | $\sigma_{rz}^2 \times \Delta T$ | 1.432e-6 <i>deg</i> |
| $Q_{4,4}$ | rz_{walk} | 0.001 <i>deg/s</i> |
| $Q_{5,5}$ | GPS_N | 1e-6 <i>m</i> |
| $Q_{6,6}$ | GPS_E | 1e-6 <i>m</i> |
| $Q_{7,7}$ | $\sigma_{ax}^2 \times \Delta T$ | 4.3121e-6 <i>m/s</i> |
| $Q_{8,8}$ | ax_{walk} | 0.01 <i>m/s²</i> |
| $Q_{9,9}$ | $\sigma_{rz}^2 \times \Delta T$ | 1.432e-6 <i>deg</i> |
| $Q_{10,10}$ | rz_{walk} | 0.001 <i>deg/s</i> |
| $Q_{11,11}$ | GPS_N | 1e-6 <i>m</i> |
| $Q_{12,12}$ | GPS_E | 1e-6 <i>m</i> |

Table 5.11: Measurement Noise Covariance

| Position | Parameter | Value |
|-------------|----------------------|----------------------|
| $R_{1,1}$ | $\sigma_{V_{GPS}}^2$ | 0.0025 <i>m/s</i> |
| $R_{2,2}$ | $\sigma_{V_{WS}}^2$ | 7.2082e-7 <i>m/s</i> |
| $R_{3,3}$ | σ_{ψ}^2 | 1e4 <i>deg</i> |
| $R_{4,4}$ | $\sigma_{GPS_N}^2$ | 3.356 <i>m</i> |
| $R_{5,5}$ | $\sigma_{GPS_E}^2$ | 2.4183 <i>m</i> |
| $R_{6,6}$ | $\sigma_{V_{GPS}}^2$ | 0.0025 <i>m/s</i> |
| $R_{7,7}$ | $\sigma_{V_{WS}}^2$ | 7.2082e-7 <i>m/s</i> |
| $R_{8,8}$ | σ_{ψ}^2 | 1e4 <i>deg</i> |
| $R_{9,9}$ | $\sigma_{GPS_N}^2$ | 2.7726 <i>m</i> |
| $R_{10,10}$ | $\sigma_{GPS_E}^2$ | 3.8801 <i>m</i> |
| $R_{11,11}$ | σ_r^2 | 1.2000e-5 <i>m</i> |
| $R_{12,12}$ | σ_{ϕ}^2 | 1 <i>deg</i> |

The variance of the heading measurement used in $R_{3,3}$ and $R_{8,8}$ is a function of velocity and is defined by Equation 5.4. A logic switch is employed to prevent a division by zero error when the velocity drops below 0.001 m/s and 1e4 is used.

5.4.2 Simulated Dynamic Lead with Static Trail

A second scenario evaluates the ability of the relative position estimator to estimate the positions and headings of one moving and one stationary UGV. The lead UGV started at the origin and accelerated to 7.5 m/s along a heading of 45 degrees while the trail UGV remained stationary. The simulated top speed exceeds the normal operating speed of

the MATILDA but was selected to ensure the estimator could function past the operating range of the UGV. The estimator successfully estimated the position and heading of the lead UGV. Figure 5.30 compares the GPS position measurements to the estimated positions for both UGVs. The position error is shown in Figure 5.31 for comparison to the error of the navigation estimator. The position error is shown in Figure 5.31 for comparison to the error of the navigation estimator. The position error of the lead UGV is less than the error present in the trail UGV estimate up to 15 seconds. This trend matches expectations with the inclusion of the additional relative measurements. After 15 seconds, the error in the lead estimate becomes more erratic and exceeds the error of the trail estimate.

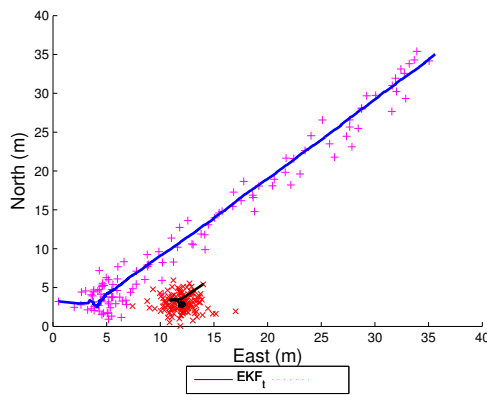


Figure 5.30: Simulated Dynamic/Static Position Estimate

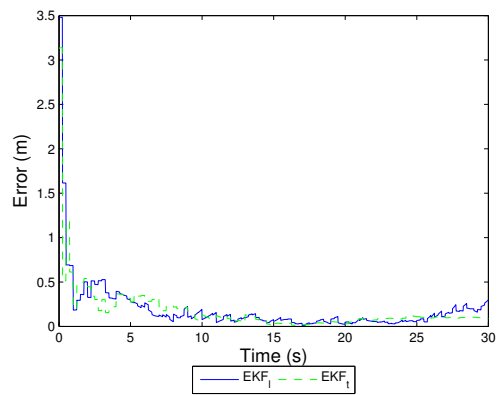


Figure 5.31: Simulated Dynamic/Static Position Error

The increase in error can be attributed to the distance separating the UGVs at this point. At 15 seconds, the relative range between the UGVs is 12.5 m and the range linearly increases up to 50 m by the end of the run. The noise characteristics of the range and bearing are modeled as additive, white and Gaussian with fixed variations. As the range increases, the error introduced by the bearing measurement represents a larger and larger portion of the position estimate. The relative range and hence position are a function

of the range and bearing measurements. The increase in noise in the measurements yields additional error in the corresponding estimate. The ultrasonic sensors are unable to operate at ranges past 6 meters, and the error introduced at greater ranges is thus neglected. The focus of the thesis has been to determine relative position of the UGVs in close proximity.

The dynamic platform ensured GPS position measurements were available to bound the heading error for the lead UGV. A comparison of the heading estimates for both UGVs are shown in Figure 5.32. The additional measurements provide only marginal gains in performance for the heading of the lead UGV. The precision of the ultrasonic sensors are offset by the low update rate. The heading error shown in Figure 5.33 illustrates this point. The main gains achieved by the additional measurements occur in the position refinement when the lead UGV is moving.

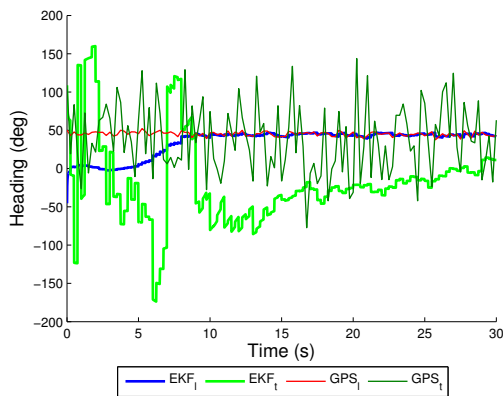


Figure 5.32: Simulated Dynamic/Static Heading Estimate

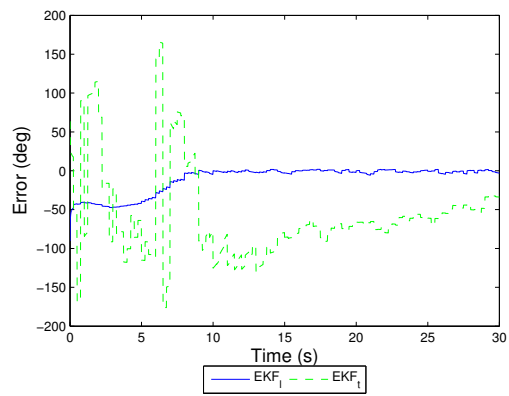


Figure 5.33: Simulated Dynamic/Static Heading Error

A comparison of the mean error and standard deviation for simulated straight line data is provided in Table 5.12. A significant decrease in the position error is seen. The heading

error is comparable for the navigation and the relative position estimator. The values are calculated after the filter settles to accurately reflect the steady state performance.

Table 5.12: Simulated Linear Estimate Error and Standard Deviation

| | $mean_{position}$ | $\sigma_{position}$ | $mean_{heading}$ | $\sigma_{heading}$ |
|----------------------|-------------------|---------------------|------------------|--------------------|
| Navigation Estimator | 0.25 m | 0.14112 m | -0.214 deg | 1.6818 deg |
| Relative Estimator | 0.1364 m | 0.1225 m | -0.379 deg | 1.719 deg |

5.4.3 Simulated Dynamic Lead with Dynamic Trail

A final simulation evaluated the estimator’s performance while both UGVs are moving. The UGVs maintained the same speed and heading to mimic traveling in formation. The UGVs traveled along parallel paths with the UGVs separated by 4 meters both laterally and longitudinally. Figure 5.34 shows the position estimates during the simulation. The estimates are initially erratic due to the exclusion of faulty GPS heading measurements. The EKF was able to estimate the position of both UGVs to within half a meter after several seconds of measurements. The error of the position estimates is shown in Figure 5.35. The minimum error achieved is 8 cm; however, the mean lead error is 14.2 cm and the mean trail error is 21.1 cm. The standard deviation for the lead and trail error is 11.7 cm and 5.85 cm respectively. The mean value of the error is a function of the noise introduced with each measurement. Reduction of the error requires less noise to be introduced into the system via higher quality measurements or increase the number of measurements available.

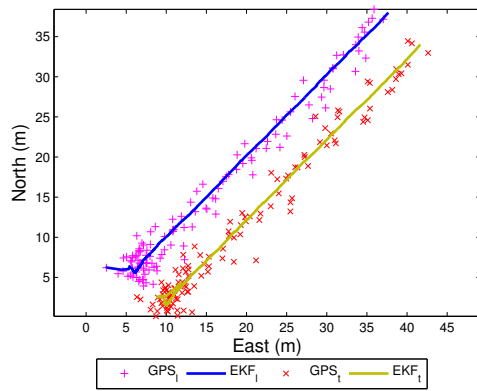


Figure 5.34: Simulated Dynamic/Dynamic Position Estimate

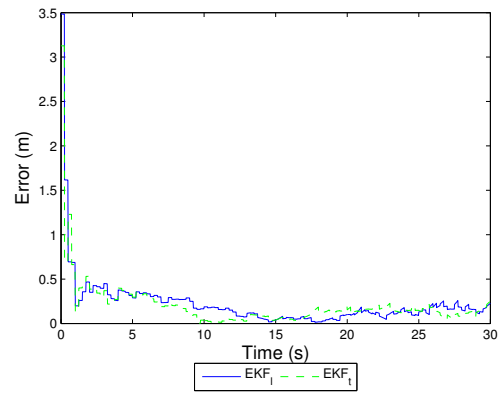


Figure 5.35: Simulated Dynamic/Dynamic Position Error

The inclusion of the relative measurements visibly alters the response of the estimator. Figure 5.36 compares the estimated headings of the trail and lead UGV. The lead estimate converges smoothly from the initial value to the actual heading. The process takes approximately five seconds, which represents five sets of relative measurements. The trail estimate overshoots the actual heading twice before settling to the actual value. Figure 5.37 compares the error present in both estimates over time.

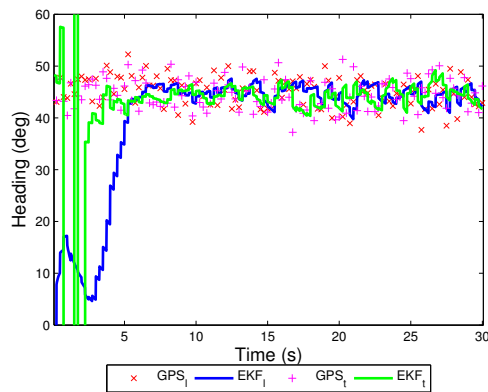


Figure 5.36: Simulated Dynamic/Dynamic Heading Estimate

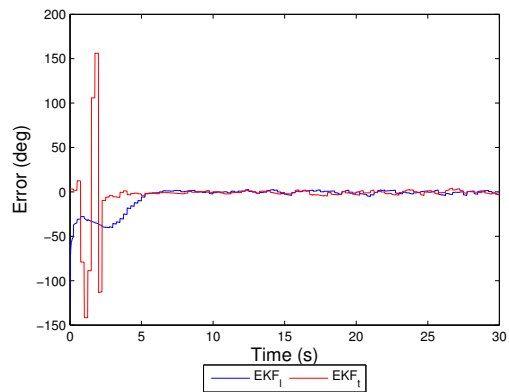


Figure 5.37: Simulated Dynamic/Dynamic Heading Error

5.4.4 Experimental Performance

Once the EKF was successfully evaluated with simulated data, actual data received from both sensor suites was evaluated. The experimental data was collected simultaneously from both sensor suites and the UTC field was used to line up measurements. The estimates for each UGV vary due to the noise unique to each sensor's measurements.

Static/Static Experimental Tests

The same test procedure from Section 5.3.3 was used to evaluate the static performance using the experimental system. The trail position estimate for the UGVs showed improvement over the estimate from the navigation estimator. The results matched the simulated results for both UGVs. The estimator is able to effectively use the additional measurements to refine the position estimate.

The position estimates of the lead and trail UGV are shown in Figure 5.38. The estimates converge to values along the same east value and are properly spaced based on the actual spacing of the robots. The estimate provided using the actual data from the sensors illustrates how the noise present in the measurements affects the estimate. The simulation used a Gaussian white distribution to replicate noise on the GPS measurements. The noise in the actual GPS measurements is slightly colored and the error present in the estimate reflects this characteristic. The estimate does converge, but meanders as it approaches the steady state value in the same manner as the GPS measurements. The presence of colored noise violates one of the assumptions of the EKF and the resulting estimate includes slightly higher error. The resulting estimate is not optimal but does represent a much better result than could be achieved with a single measurement or input.

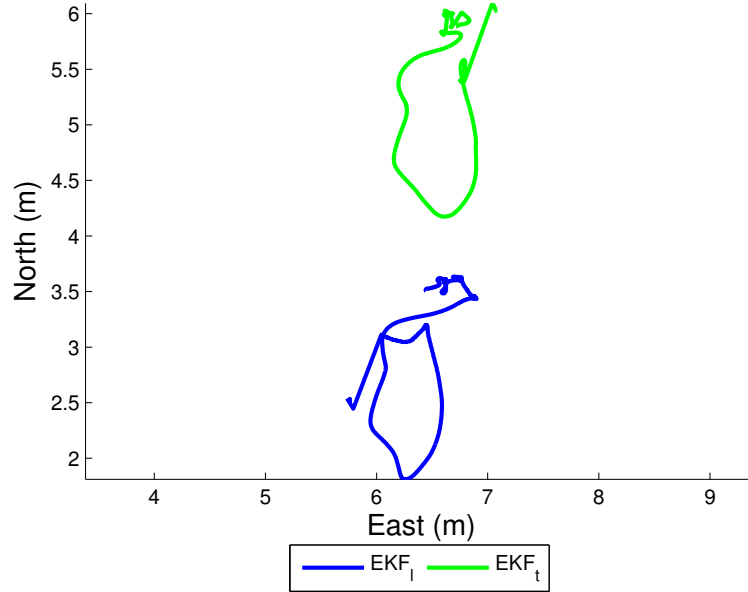


Figure 5.38: Experimental Static/Static Position Estimate

The standard deviation of the position estimates are provided in Table 5.13. The values previously presented in Table 5.8 are included for comparison. The most significant improvement can be seen when comparing the standard deviations for the trail unit.

Table 5.13: Noise Characteristics Comparison of Estimator Position Standard Deviation

| | Navigation Estimator | | Relative Estimator | |
|--------------------|----------------------|------------|--------------------|------------|
| | σ_N | σ_E | σ_N | σ_E |
| Simulated | 0.4197 m | 0.3507 m | 0.5326 m | 0.4521 m |
| Experimental Lead | 0.434 m | 0.2659 m | 0.4848 m | 0.2495 m |
| Experimental Trail | 0.6249 m | 0.2069 m | 0.4890 m | 0.1793 m |

A comparison of the heading estimates from the same run are shown in Figure 5.39. The heading estimate of the lead UGV converges to zero and dithers about the value for the entire ten minute run. The variation of the experimental heading for the lead unit is slightly higher than the variation observed in the simulated runs, but the estimates are comparable. The heading estimate of the trail UGV varies over the entire run as expected due to the lack of trail heading measurements.

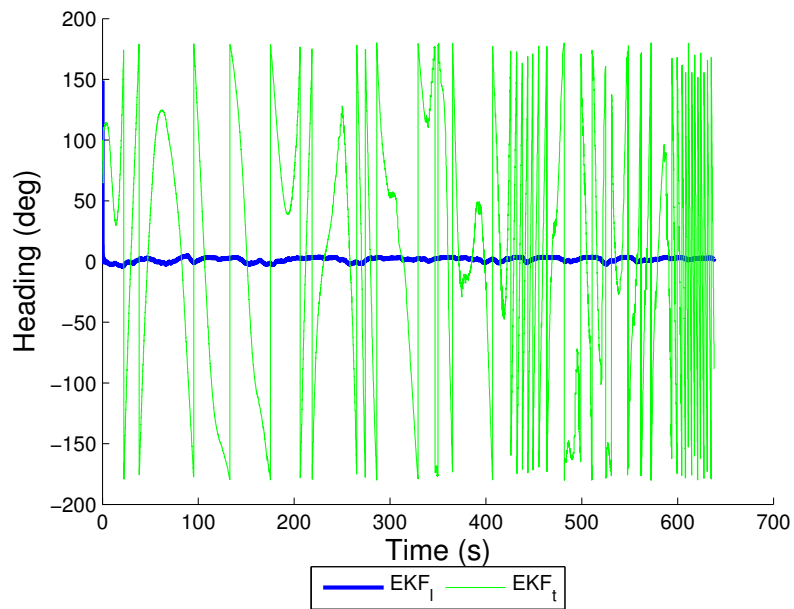


Figure 5.39: Experimental Static/Static Heading Estimate

Dynamic/Dynamic Experimental Tests

The experimental procedures outlined in Section 5.3.3 are replicated to evaluate the relative position estimator with dynamic inputs. The UGVs travel in a clockwise direction with the trail sensor suit being towed 1.34 m behind the lead UGV. The elliptical path

allows for comparison of the lead and trail estimates. Figure 5.40 compares the position estimates for both UGVs. The estimates are quite promising throughout the entire run. The trail estimate diverges at the turn in the lower left corner of the figure. Inspection of the GPS measurements provided to the respective units in Figure 5.18 and Figure 5.19 shows significantly more noise in the trail unit's measurements at that period. Comparing the estimates from both EKF's shows the increased accuracy of the estimate provided by the relative position estimator.

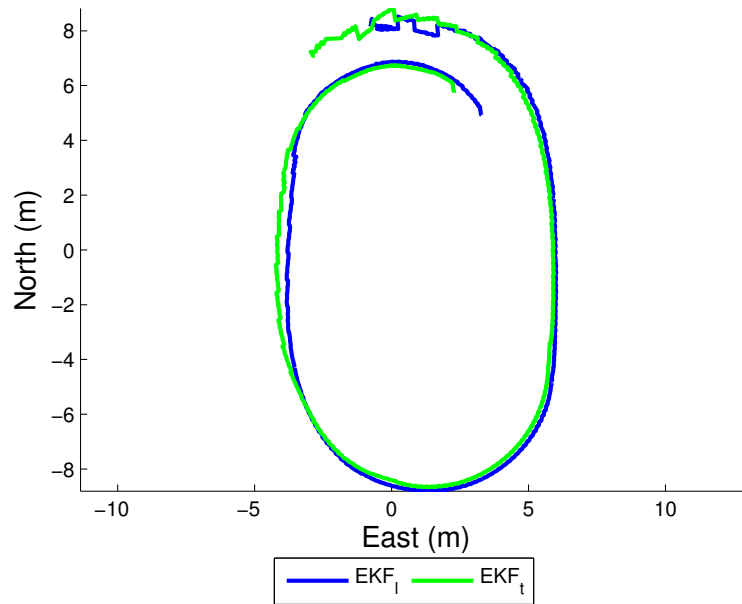


Figure 5.40: Experimental Dynamic/Dynamic Position Estimate

Figure 5.41 compares the heading estimates for both UGVs during the same period. The spikes in the heading estimate for the lead UGV are not removed but the magnitude of the spike is attenuated when compared to Figure 5.24 and Figure 5.25 from the navigation estimator estimates. The lag between the lead and trail estimate is due to the separation

maintained between the sensors. The MATILDA is traveling at 0.9 m/s. The separation of 1.34 m between units represents a time delay of 1.48 s between the lead UGV's measurements and the trail UGV's measurements from the same point on the path.

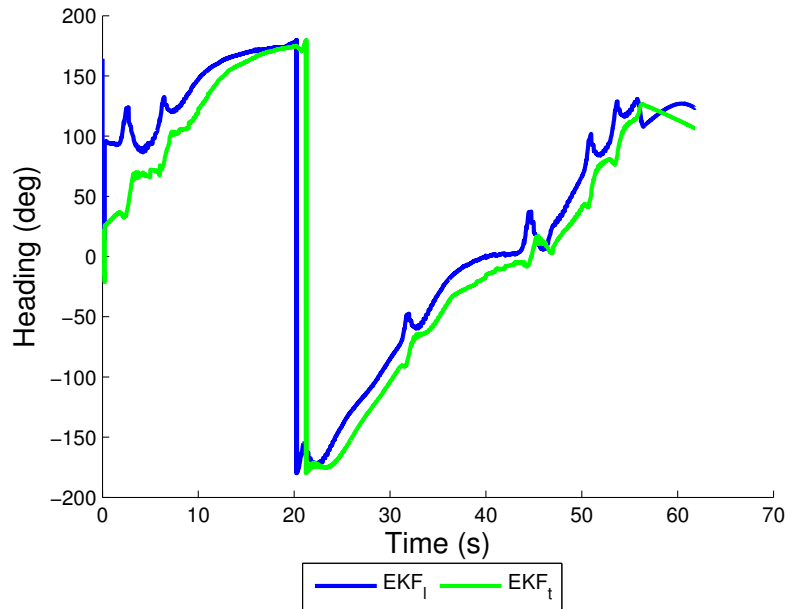


Figure 5.41: Experimental Dynamic/Dynamic Heading Estimate

A visual comparison of position estimates from the navigation estimator are shown in Figure 5.42. The position estimates are generated by separate estimators with no information included from the other UGV. The position estimates match the traveled path; however, the relative position and orientation vary over the length of the run. The position estimates from the relative position estimator are shown in Figure 5.43 for comparison.

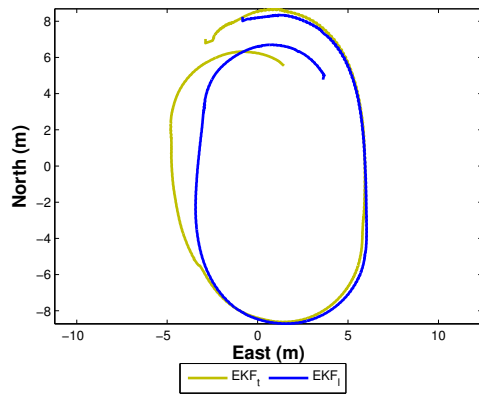


Figure 5.42: Position Estimates using Navigation Estimators

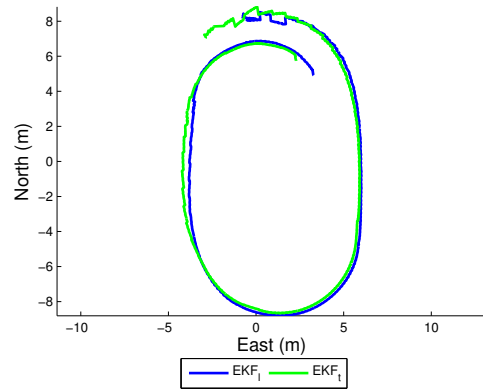


Figure 5.43: Position Estimates using Relative Position Estimator

The relative position error between the lead and trail UGV are shown in Figure 5.44. Once the relative position estimator reaches steady state after 3 seconds, the relative position error remains less than 20 cm. The mean error for the relative position estimator is 6.595 cm compared to 71.86 cm for the navigation estimator. This value represents a significant improvement for estimating relative position when compared to the values from using a pair of navigation estimators or GPS alone.

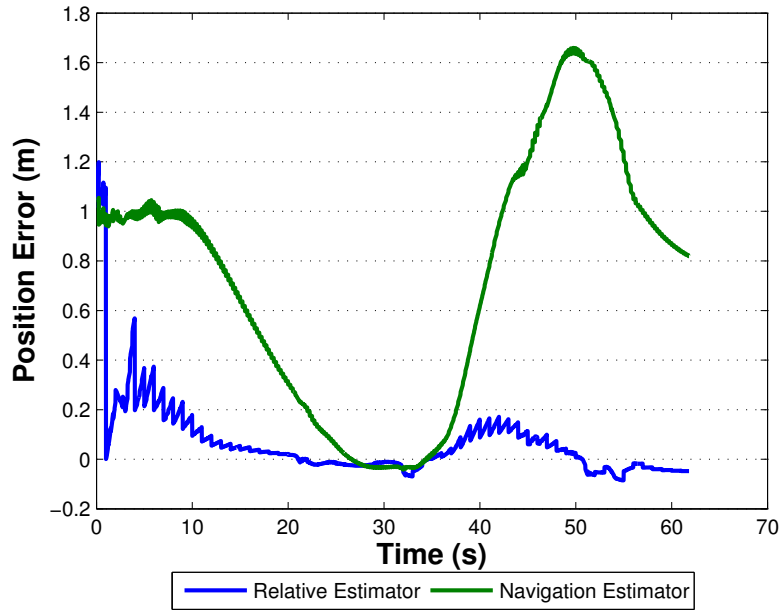


Figure 5.44: Relative Position Error on Elliptical Path

5.5 Conclusion

The Extended Kalman Filter processes noisy measurements in order to provide an optimum estimate of the states. The noise characteristics for each sensor were empirically determined and used to populate the sensor noise and process noise covariance matrices for the EKF. The performance of the navigation estimator EKF was evaluated using both simulated and experimental data with the individual estimator of Chapter 3 and the relative estimator of Chapter 4. The simulations provided insight into the estimate error under a variety of static and dynamic scenarios. The navigation EKF evaluated actual data from the lead and trail sensor packages to ensure proper operation of the estimator and the sensor

packages. The estimates from the position navigator served as base lines for comparison of the relative position estimator.

The relative position estimator was evaluated using the same simulated and experimental data. The simulations provided insight into the performance of the EKF and the lower limit for error that could be expected in the provided estimates. A visible improvement in the heading and position estimates can be seen when compared to the navigation estimates. The inherent limitation of estimating heading while stationary was not overcome; however, the relative measurements do provide additional information about the orientation and position of the UGVs when static. The inclusion of the additional shared measurements was shown to improve the fidelity of the position estimates. The relative position error was reduced an order of magnitude by using the relative position estimator.

6.1 Summary of Contributions

This thesis has shown how relative measurements can be used to improve position and heading estimates for control of multiple UGVs. Ultrasonic sensors were employed in a novel manner to provide relative range and bearing measurements between a pair of UGVs in an outdoor environment. A low cost GPS receiver provided an ultraprecise Pulse Per Second (PPS) signal to synchronize the ultrasonic sensors on each UGV. The common time provided by the PPS allowed the sensors to reliably provide measurements in a noisy outside environment.

A navigation estimator based on an Extended Kalman Filter was also developed to provide position and heading estimates. The filter used inputs and measurements from a MEMS based IMU, track sensors, and GPS receiver. The navigation estimator outputs provided the baseline for comparison of the relative position estimator. Simulated static and dynamic data was used to test the performance of the algorithm to ensure proper operation and baseline values for later comparison. The navigation estimator provided the base algorithm for the relative position estimator.

The PPS triggered ultrasonic sensor concept was implemented and validated to ensure the selected components would reliably provide range and bearing measurements. Experimental testing demonstrated that the concept reliably provided measurements with precision that was comparable to the other sensors. The primary concern associated with the measurements was the slower output rate of 1 Hz.

The relative position estimator developed was an extension of the navigation estimator that uses the global measurements from both UGVs and the relative measurements of their position and orientation. The use of the shared measurements yielded a higher fidelity position and heading estimate under many conditions. The position estimates improved under both static and dynamic conditions when compared to the navigation estimator. The heading estimates improved when the GPS provided heading measurements. The inability of the GPS to provide course measurements when stationary prevented the EKF from providing a meaningful heading estimate for static data. This limitation is present in both estimators due to lack of observability of that state.

The research presented the performance gains that can be achieved with relative measurements and a concept to provide them. The noise present in the measurements limit the precision of the estimates provided by the EKF. Additional work is required to refine the concept and the implementation of the relative position estimator. Additional work is required to fully explore the gains in performance that can be achieved using ultrasonic sensors to provide relative measurements of UGV position and orientation.

6.2 Future Work

The first avenue of future work is to implement the relative position estimator in real time to allow for use in a controller for the UGV. This nontrivial task requires the algorithm to be transferred from MATLAB to C++. The current algorithm is used in post process and does not have the same time constraints that will be imposed on the real time version. The mathematical operations required and the memory necessary are within the capabilities

of current computer technology, but significant development will be required to ensure the algorithm runs properly.

Another avenue of future work is to investigate the problems and performance gains achieved by implementing the relative position estimator with a cascaded filter approach. The use of several smaller filters would reduce the computational burden. The correlation of noise in the estimates would require further investigation as discussed in Section 4.2. Reducing the computational cost of the algorithm will also aid in real time implementation.

Further work is also needed to overcome the estimator's inability to measure heading. This limitation stems from the inability of a single antennae GPS receiver to measure course when the UGV is not moving. The use of a dual antennae GPS system could provide this measurement. The dual antennae system could also be used to measure heading in addition to course. The inclusion of heading measurements when stationary would allow for estimation of initial heading. This approach would require additional hardware and additional operations within the algorithm.

Another avenue for further work is investigating the affect of increasing the relative measurement rate. The RCM4100 clock synchronized with the PPS could be used to generate a higher frequency signal for the ultrasonic sensors. The drift of the clock on the RCM4100 would introduce noise into the relative measurements; however, the magnitude may be small enough to warrant the use of the higher measurement rate. uBlox recently introduced a receiver that provides a 10 PPS signal that would provide the higher rate without the noise introduced by the RCM4100 clock. The effect on the IMU would have to be evaluated since its design is based on a 1 Hz PPS signal. The higher rate may cause conflicts with the embedded IMU processor. Both solutions provide a higher measurement

rate; however, evaluation of the performance based on the rate is also necessary to ensure the selected rate complements the other measurements and system dynamics.

The inclusion of a bearing measurement from the trail to the lead UGV warrants investigation as well. The inclusion of range and bearing measurements from the trail unit should yield performance similar to the position and heading estimates of the lead unit. The increase in performance must also be evaluated based on the increased computational burden necessary to implement the larger estimator.

BIBLIOGRAPHY

- [1] E. Abbott and D. Powell, *Land-vehicle navigation using gps*, Proceedings of the IEEE, vol. 87, IEEE, January 1999, pp. 145–162.
- [2] L. Angrisani, A. Baccigalupi, and R. Schiano Lo Moriello, *A measurement method based on kalman filtering for ultrasonic time-of-flight estimation*, Instrumentation and Measurement, IEEE Transactions on **55** (April 2006), no. 2, 442–448.
- [3] Z. Berman and J.D. Powell, *The role of dead-reckoning and inertial sensors in future general aviation navigation*, Proceedings of the 1998 IEEE Position Location and Navigation Symposium, 1998, pp. 510–517.
- [4] D. M. Bevly, *Global positioning system (gps): A low-cost velocity sensor for correcting inertial sensor errors on ground vehicles*, Journal of Dynamic Systems, Measurement, and Control **126** (2004), 255–264.
- [5] J. J. Biesiadecki, P. C. Leger, and M. W. Maimone, *Tradeoffs between directed and autonomous driving on the mars exploration rovers*, The International Journal of Robotics Research **26** (2007), 91–104.
- [6] J. Borenstein and L. Feng, *Measurement and correction of systematic odometry errors in mobile robots*, IEEE Transactions on Robotics and Automation **12** (1996), no. 6.
- [7] J. Borenstein and Y. Koren, *Obstacle avoidance with ultrasonic sensors*, Robotics and Automation, IEEE Journal of [see also IEEE Transactions on Robotics and Automation] **4** (Apr 1988), no. 2, 213–218.
- [8] R. Daily and D.M. Bevly, *The use of gps for vehicle stability control systems*, IEEE Transactions on Industrial Electronics **51** (2004), no. 2, 270–277.
- [9] G. Dedes, R. Da and K. Shubert, *Design and analysis of a high-accuracy airborne gps/ins system*, Proceedings of the 9th International Technical Meeting of the Satellite Division of The Institute of Navigation, September 1996, pp. 955–964.
- [10] Defense Advanced Research Projects Agency, Arlington, VA, *Urban challenge rules*, October 27 2007.
- [11] D. W. Gage, *Ugv history 101: A brief history of ummaned ground vehicle (ugv) development efforts*, Ummaned Systems Magazine **13** (1995).

- [12] S. Godha and M.E. Cannon, *Integration of dgps with a low cost mems-based inertial measurement unit (imu) for land vehicle navigation applications*, Proceedings of the ION GNSS (Long Beach, CA), ION, September 2005.
- [13] J.L. Jones, *Robots at the tipping point: the road to irobot roomba*, Robotics & Automation Magazine, IEEE **13** (2006), no. 1, 76–78.
- [14] H. Kuttruff, *Room acoustics*, 2nd ed., Applied Science Publishers, 1979.
- [15] W. Lewandowski and C. Thomas, *Gps time transfer*, Proceedings of the IEEE **79** (Jul 1991), no. 7, 991–1000.
- [16] J.L. Martinez, A. Mandow, J. Morales, A. Garcia-Cerezo, and S. Pedraza, *Kinematic modelling of tracked vehicles by experimental identification*, Proc. IEEE/RSJ International Conference on Intelligent Robots and Systems (IROS 2004), vol. 2, 28 Sept.–2 Oct. 2004, pp. 1487–1492.
- [17] Mesa Associates, Inc, Madison, AL, *Operator’s and maintenance manual*, April 2004.
- [18] S. Panzieri, F. Pascucci, and G. Ulivi, *An outdoor navigation system using gps and inertial platform*, IEEE/ASME Transactions on Mechatronics **7** (2002), no. 2.
- [19] B.W. Parkinson and J.J. Spilker (eds.), *Global positioning system: Theory and applications*, vol. I, AIAA, 1996.
- [20] Rabbit Semiconductor, *Rcm4100 rabbitcore user’s manual*, 2007.
- [21] S.I. Roumeliotis and G.A. Bekey, *Collective localization: a distributed kalman filter approach to localization of groups of mobile robots*, Proc. IEEE International Conference on Robotics and Automation ICRA '00, vol. 3, 24–28 April 2000, pp. 2958–2965.
- [22] D. Rubinstein and R. Hitron, *A detailed multi-body model for dynamic simulation of off-road tracked vehicles*, Journal of Terramechanics **41** (2004), 163–173.
- [23] J.E. Shigley and J.J. Uicker, *Theory of machines and mechanism*, 2nd ed., McGraw-Hill series in mechanical engineering, McGraw-Hill, 1995.
- [24] B. Skylar, *Digital communications*, 2nd ed., Prentice Hall PTR, 2004.
- [25] R.F. Stengel, *Optimal control and estimation*, Dover books on advanced mathematics, Dover Publications, New York, 1994.
- [26] T. Tanzawa, N. Kiyohiro, S. Kotani, and H. Mori, *The ultrasonic range finder for outdoor mobile robots*, Intelligent Robots and Systems 95. 'Human Robot Interaction and Cooperative Robots', Proceedings. 1995 IEEE/RSJ International Conference on **3** (5-9 Aug 1995), 368–373 vol.3.

- [27] J. Yang and J. Kim, *Sliding mode control for trajectory tracking of nonholonomic wheeled mobile robots*, IEEE Transactions on Robotics and Automation **15** (1999), no. 3, 578–587.

APPENDIX A
NOMENCLATURE

NOMENCLATURE

| | |
|-----------|--|
| \dot{E} | East component of velocity vector in global ENU frame |
| \dot{N} | North component of velocity vector in global ENU frame |
| \dot{X} | First derivative of state |
| λ | Wavelength |
| ψ | Heading |
| a_b | Accelerometer Bias |
| B | Input Matrix |
| C | Observation Matrix |
| c | Speed of sound |
| E | Position of robot in North direction |
| f | Frequency |
| g_b | Rate Gyro Bias |
| J | Jacobian |
| L_k | Filter gain |
| N | Position of robot in North direction |
| P | Covariance Matrix |

| | |
|-------|--|
| u | Inputs to system |
| V_x | Longitudinal velocity of robot |
| V_x | X component of velocity vector in body fixed frame |
| x | State matrix |
| Y | Measurements of system |